

INVERSEBENCH: BENCHMARKING PLUG-AND-PLAY DIFFUSION MODELS FOR SCIENTIFIC INVERSE PROBLEMS

Anonymous authors

Paper under double-blind review

ABSTRACT

Plug-and-play diffusion models have emerged as a promising research direction for solving inverse problems. However, current studies primarily focus on natural image restoration, leaving the performance of these algorithms in scientific inverse problems largely unexplored. To address this gap, we introduce INVERSEBENCH, a framework that evaluates diffusion models across five distinct scientific inverse problems. These problems present unique structural challenges that differ from existing benchmarks, arising from critical scientific applications such as black hole imaging, seismology, optical tomography, medical imaging, and fluid dynamics. With INVERSEBENCH, we benchmark 14 inverse problem algorithms that use plug-and-play diffusion models against strong, domain-specific baselines, offering valuable new insights into the strengths and weaknesses of existing algorithms. We open-source the datasets, pre-trained models, and the codebase to facilitate future research and development.

1 INTRODUCTION

Inverse problems are fundamental in many domains of science and engineering, where the goal is to infer the unknown source from indirect and noisy observations. Example domains include astronomy (Chael et al., 2019), geophysics (Virieux & Operto, 2009), optical microscopy (Choi et al., 2007), medical imaging (Lustig et al., 2007), fluid dynamics (Iglesias et al., 2013), among others. These inverse problems are often challenging due to their ill-posedness, complexity in the underlying physics, and unknown measurement noise.

The use of diffusion models (DMs) (Sohl-Dickstein et al., 2015; Dhariwal & Nichol, 2021) for solving inverse problems has become increasingly popular. One attractive approach is plug-and-play diffusion models to use the DM as a plug-and-play prior (Wang et al., 2022; Dou & Song, 2024), where the inference objective is decomposed into the prior (using a pre-trained diffusion model) and the likelihood of fitting the observations (using a suitable forward model). The advantage of this idea is twofold: (1) As a powerful class of generative models, DMs can efficiently encode the complex and high-dimensional prior distribution, which is essential to overcome ill-posedness. (2) As plug-and-play priors, DMs can accommodate different problems without any re-training by decoupling the prior and likelihood. However, current algorithms are primarily evaluated and compared on a fairly narrow set of image restoration tasks such as inpainting, super-resolution, and deblurring (Song et al., 2023a; Mardani et al., 2024). These problems differ greatly from those from science and engineering applications such as geophysics (Virieux & Operto, 2009), astronomy (Porth et al., 2019), oceanography (Carton & Giese, 2008), and many other fields, which have very different structural challenges arising from the underlying physics. It is unclear how much insight can be carried over from image restoration to scientific inverse problems.

In this paper, we introduce INVERSEBENCH, a comprehensive benchmarking framework designed to evaluate PnP diffusion prior approaches in a systematic and easily extensible manner. We curate a diverse set of five inverse problems from distinct scientific domains: optical tomography, black hole imaging, medical imaging, seismology, and fluid dynamics. These problems present structural challenges that differ significantly from natural image restoration tasks (cf. Figure 1 and Table 2), and encompass a broad spectrum of complexities across multiple scientific fields. Most notably, the

054
055
056
057
058
059
060
061
062
063
064
065
066
067
068
069
070
071
072
073
074
075
076
077
078
079
080
081
082
083
084
085
086
087
088
089
090
091
092
093
094
095
096
097
098
099
100
101
102
103
104
105
106
107

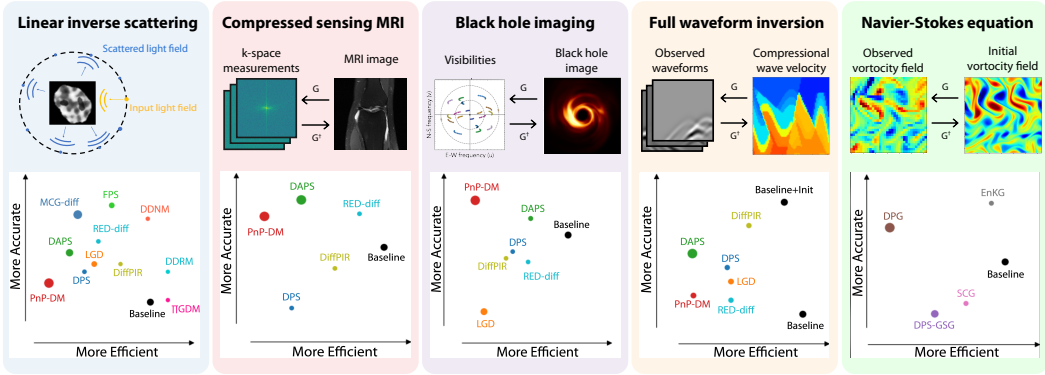


Figure 1: Illustration of five benchmark problems in the INVERSEBENCH. G represents the forward model that produces observations from the source. G^{-1} represents the inverse map. In the linear inverse scattering problem (left two), the observation is the recorded data from the receivers and the unknown source we aim to infer is the permittivity map of the object. The bottom panel displays the efficiency and accuracy plots for our benchmarked algorithms. Certain characteristics of the problem cause the efficiency and accuracy trade-offs of each algorithm to vary across tasks. In these plots, the larger radius of the points indicates greater interaction with the forward function G , as measured by the number of forward model evaluations.

forward model (which maps the source to observations) is defined using various types of physics-based models which can be highly non-linear and difficult to evaluate.

We select 14 representative plug-and-play diffusion model algorithms proposed for solving inverse problems, providing a thorough comparison of their performance across different scientific inverse problems and further insights into their efficacy and limitations. Additionally, we establish strong, domain-specific baselines for each inverse problem, providing a meaningful reference point for assessing the effectiveness of diffusion model-based approaches against traditional methods.

Through extensive experiments, we find that PnP diffusion prior methods generally exhibit strong performance given a suitable dataset for training a diffusion prior. This performance is consistent even as we vary the forward model (which is a strength of a PnP approach), given appropriate tuning. However, for forward models that require certain constraints on the input (e.g., uses a PDE solver), performance can be very sensitive to hyperparameter tuning. Moreover, the strength of using a diffusion prior can also be a limitation, as PnP diffusion prior methods have difficulty when the source image is out of the prior distribution (i.e., the use of diffusion models makes it difficult to recover “surprising” results). Additionally, we find that PnP methods that use multiple queries of the forward model tend to outperform simpler methods like DPS, at the cost of requiring additional tuning and computation, which points to an interesting direction for future method development.

INVERSEBENCH is implemented as a highly modular framework that can interface with new inverse problems and algorithms to run experiments at scale. We will open source the datasets, pre-trained models, and the codebase, to facilitate reproducibility and accelerate the development of more effective techniques in solving inverse problems.

2 PRELIMINARIES

2.1 INVERSE PROBLEMS

Following the typical setup, we have *observations* $\mathbf{y} \in \mathbb{C}^m$ from an unknown source $\mathbf{z} \in \mathbb{C}^n$ via a *forward model* $G : \mathbb{C}^n \rightarrow \mathbb{C}^m$. The inverse problem is to design a mapping G^\dagger to infer \mathbf{z} from \mathbf{y} :

$$\mathbf{z} \leftarrow G^\dagger(\mathbf{y}), \quad \text{where } \mathbf{y} = G(\mathbf{z}, \xi). \quad (1)$$

Here, ξ represents noise in the forward model. In scientific applications, G typically represents the measurement or sensing device (telescopes, infrared cameras, seismometers, electron microscopes,

etc.). Typical inverse problems present four major challenges: (1) Many inverse problems are ill-posed, meaning that a solution may not exist, may not be unique, or may not be stable (Hadamard, 2014). For example, in black hole imaging, there could be multiple solutions that match the same sparse measurements. (2) The measurement noise is generally not separately observed (it is part of the observations \mathbf{y}), and accounting for it in the inverse problem can be challenging, especially for poorly characterized noise profiles (e.g., not Gaussian). (3) The forward model might be highly nonlinear and lack a closed-form expression, leading to computational and numerical challenges in method design. (4) Designing an appropriate prior for the unknown source is also a critical challenge. For some problems, it is necessary for the designed prior to capture the complex structure of the solution space while remaining computationally tractable.

All these challenges necessitate some kind of regularization. While classic optimization approaches often employ simple regularizers (e.g., local isotropic smoothness), these fail to capture global or anisotropic properties. The use of diffusion models as a prior is attractive as a way to capture these more complex properties.

2.2 DIFFUSION MODELS

Diffusion models are a powerful class of deep generative models that can capture complicated high-dimensional distributions such as natural images (Rombach et al., 2022), proteins (Fu et al., 2024), small molecules (Luo et al., 2024), robotic trajectories (Chi et al., 2023), amongst other domains. Given their strong performance and compatibility with Bayesian inference, using diffusion models to model the solution space as a prior is a promising idea (Song et al., 2020; Chung et al., 2023; Song et al., 2022).

We consider the continuous formulation of diffusion models proposed by Song et al. (2020), which expresses the forward diffusion and backward denoising process as stochastic differential equations (SDEs). The forward process transforms a data distribution $\mathbf{x}_0 \sim p_{\text{data}}$ into an approximately Gaussian one $\mathbf{x}_T \sim \mathcal{N}(0, \sigma^2(T)\mathbf{I})$ by gradually adding Gaussian noise according to:

$$d\mathbf{x}_t = f(\mathbf{x}_t, t)dt + g(t)d\mathbf{w}_t, \quad (2)$$

where f is a predefined vector-valued drift, g is the diffusion coefficient, \mathbf{w} is the standard Wiener process with time t flowing from 0 to T . The backward process sequentially denoises the Gaussian noise into clean data, which is given by the reverse-time SDE:

$$d\mathbf{x}_t = \left(f(\mathbf{x}_t, t) - \frac{1}{2}g^2(t)\nabla_{\mathbf{x}_t} \log p_t(\mathbf{x}_t) \right) dt + g(t)d\bar{\mathbf{w}}_t, \quad (3)$$

where $p_t(\mathbf{x}_t)$ is the probability density of \mathbf{x}_t at time t and $\bar{\mathbf{w}}_t$ is the reverse-time Wiener process. The diffusion model is trained to learn the score function $\nabla_{\mathbf{x}_t} \log p_t(\mathbf{x}_t)$. Once trained, the diffusion model can generate new samples from the learned data distribution by solving (3).

2.3 PLUG-AND-PLAY DIFFUSION MODELS FOR INVERSE PROBLEMS

We use the term *Plug-and-Play Diffusion Prior* (PnPDP) to refer to the class of recent methods that use diffusion models (or the denoising network within) as plug-and-play priors (Venkatakrishnan et al., 2013) for solving inverse problems. The basic idea is to either modify or use (3) to generate samples from $p(\mathbf{x}|\mathbf{y})$ rather than the prior $p(\mathbf{x})$, which under Bayes rule can be expressed as $p(\mathbf{x}|\mathbf{y}) \propto p(\mathbf{x})p(\mathbf{y}|\mathbf{x})$. The first term $p(\mathbf{x})$ can be modeled using a diffusion prior, and the second term $p(\mathbf{y}|\mathbf{x})$ can be computed using the forward model. Broadly speaking, existing PnPDP approaches can be grouped into four categories described below. Table 1 lists the 14 representative algorithms we selected, and notes their different requirements on the forward model. To avoid confusion, we use Courier font when referring to a specific algorithm in the main text throughout the paper (e.g., PnP-DM for Wu et al. (2024)).

Guidance-based methods Arguably the most popular approach to solving inverse problems with a pretrained diffusion model is guidance-based methods (Song et al., 2023a; Wang et al., 2022; Kwar et al., 2022; Rout et al., 2023; Chung et al., 2023), which modify (3) by adding a likelihood score term, $\nabla_{\mathbf{x}_t} \log p_t(\mathbf{y}|\mathbf{x}_t)$, along the diffusion trajectory. This term is related to the forward model G if the final clean \mathbf{x}_0 is a candidate source \mathbf{z} , in which case $p(\mathbf{y}|\mathbf{x}_0)$ can be estimated by querying G . However, $\log p_t(\mathbf{y}|\mathbf{x}_t)$ is generally intractable so various approximations have been proposed (Song et al., 2022; Chung et al., 2023; Song et al., 2023a; Boys et al., 2023).

Table 1: Requirements on the forward model of the algorithms evaluated in our experiments.

Category	Method	SVD	Pseudo inverse	Linear	Gradient
Linear guidance	DDRM (Kawar et al., 2022)	✓	✓	✓	–
	DDNM (Wang et al., 2022)	✗	✓	✓	–
	ΠGDM (Song et al., 2023a)	✗	✓	✗	–
General guidance	DPS (Chung et al., 2023)	✗	✗	✗	✓
	LGD (Song et al., 2023b)	✗	✗	✗	✓
	DPG (Tang et al., 2023)	✗	✗	✗	✗
	SCG (Huang et al., 2024)	✗	✗	✗	✗
	EnKG (Zheng et al., 2024)	✗	✗	✗	✗
Variable-splitting	DiffPIR (Zhu et al., 2023)	✗	✗	✗	✓
	PnP-DM (Wu et al., 2024)	✗	✗	✗	✓
	DAPS (Zhang et al., 2024)	✗	✗	✗	✓
Variational Bayes	RED-diff (Mardani et al., 2023)	✗	✗	✗	✓
Sequential Monte Carlo	FPS (Dou & Song, 2024)	✗	✗	✓	–
	MCGDiff (Cardoso et al., 2024)	✓	✓	✓	–

Table 2: Characteristics of different inverse problems in INVERSEBENCH, from left to right: whether the forward model is linear, whether one can compute the SVD from the forward model, whether the inverse problem operates in the complex domain, whether the forward model can be solved in closed form, whether one can access gradients from the forward model, and the noise type.

Problem	Linear	SVD	Complex domain	Closed-form forward	Gradient access	Noise type
Linear inverse scattering	✓	✓	✓	✓	✓	Gaussian
Compressed sensing MRI	✓	✗	✓	✓	✓	Real-world
Black hole imaging	✗	✗	✗	✓	✓	Non-additive
Full waveform inversion	✗	✗	✗	✗	✓	Noise-free
Navier-Stokes equation	✗	✗	✗	✗	✗	Gaussian

Variable splitting Variable splitting is a widely used strategy for solving regularized optimization problems and conducting Bayesian inference (Vono et al., 2019; Chen et al., 2022; Lee et al., 2021). The core idea is to split the inference into two alternating steps (Wu et al., 2024; Zhu et al., 2023; Li et al., 2024; Song et al., 2024; Zhang et al., 2024; Xu & Chi, 2024). The first step uses the forward model to update or sample in the neighborhood of the most recent \mathbf{x}_t . The second step runs unconditional inference on $p(\mathbf{x}_t)$, which amounts to running (3) for a small amount of time.

Variational Bayes Variational Bayes methods approximate intractable distributions such as $p(\mathbf{x}|\mathbf{y})$ using some simpler parameterized distribution q_θ (Zhang et al., 2018b). The key idea is to find a q_{θ^*} that, in a KL-divergence sense, both fits the observations \mathbf{y} and agrees with the prior $p(\mathbf{x})$. In this setting, one does not directly sample according to (3), but rather use it as a prior within a variational inference framework (Mardani et al., 2023; Feng et al., 2023; Feng & Bouman, 2024).

Sequential Monte Carlo Sequential Monte Carlo (SMC) methods draw samples iteratively from a sequence of probability distributions. These methods represent probability distributions by a set of particles with associated weights, which asymptotically converge to a target distribution following a sequence of proposal and reweighting steps. Recent works have extended SMC methods to the sequential diffusion sampling process (Wu et al., 2023; Trippe et al., 2023; Cardoso et al., 2024; Dou & Song, 2024), enabling zero-shot posterior sampling with diffusion priors. However, these methods are typically applicable only to inverse problems with linear forward models.

3 INVERSEBENCH

In this section, we introduce the formulation and specific challenges of the five scientific inverse problems considered in INVERSEBENCH: linear inverse scattering, compressed sensing MRI, black hole imaging, full waveform inversion, and the Navier-Stokes equation. The characteristics of these inverse problems are summarized in Table 2. Their computational characteristics are summarized in Figure 6. Detailed descriptions and formal definitions can be found in Appendix A.2.

Linear inverse scattering Inverse scattering is an inverse problem that arises from optical microscopy, where the goal is to recover the unknown permittivity contrast $\mathbf{z} \in \mathbb{R}^n$ from the measured scattered lightfield $\mathbf{y}_{\text{sc}} \in \mathbb{C}^m$. We consider the following formulation of inverse scattering

$$\mathbf{y}_{\text{sc}} = \mathbf{H}(\mathbf{u}_{\text{tot}} \odot \mathbf{z}) + \mathbf{n} \in \mathbb{C}^m \quad \text{where} \quad \mathbf{u}_{\text{tot}} = \mathbf{G}(\mathbf{u}_{\text{in}} \odot \mathbf{z}). \quad (4)$$

Here, matrices $\mathbf{G} \in \mathbb{C}^{n \times n}$ and $\mathbf{H} \in \mathbb{C}^{m \times n}$ are the discretized Green’s functions that model the responses of the optical system, \mathbf{u}_{in} and \mathbf{u}_{tot} are the input and total lightfields, \odot is the elementwise product, and \mathbf{n} is the *additive white Gaussian noise (AWGN)*. Since this problem is a linearized version of the general nonlinear inverse scattering problem based on the first Born approximation, we refer to it as linear inverse scattering. This problem allows us to test algorithms designed specifically for linear problems.

Compressed sensing MRI Compressed sensing MRI is a technique that accelerates the scan time of MRI via subsampling. We consider the parallel imaging (PI) setup of CS-MRI, which is widely adopted in research and practice. Mathematically, PI CS-MRI can be formulated as an inverse problem that aims to recover an image $\mathbf{z} \in \mathbb{C}^n$ from

$$\mathbf{y}_j = \mathbf{P}\mathbf{F}\mathbf{S}_j\mathbf{z} + \mathbf{n}_i \in \mathbb{C}^m \quad \text{for } j = 1, \dots, J$$

where $\mathbf{P} \in \{0, 1\}^{m \times n}$ is a subsampling operator and \mathbf{F} is the Fourier transform; \mathbf{y}_j , \mathbf{S}_j , and \mathbf{n}_j are the measurements, sensitivity map, and the AWGN of the j -th coil, respectively. Compressed sensing MRI is also a linear problem, but it poses significant challenges due to its high-dimensional nature, involvement of priors in the complex domain, and attention to fine-grained details.

Black hole imaging The measurements for black hole imaging (BHI) are obtained through Very Long Baseline Interferometry (VLBI). In this technique, each pair of telescopes (a, b) provides a *visibility* (van Cittert, 1934; Zernike, 1938): a measurement that samples the a particular spatial Fourier frequency of the source image related to the projected baseline between telescopes at time t

$$V_{a,b}^t = g_a^t g_b^t e^{-i(\phi_a^t - \phi_b^t)} \mathbf{I}_{a,b}^t(\mathbf{z}) + \boldsymbol{\eta}_{a,b}^t. \quad (5)$$

The ideal visibilities $\mathbf{I}_{a,b}^t(\mathbf{z})$, representing the Fourier component of the image \mathbf{z} , are corrupted by Gaussian thermal noise $\boldsymbol{\eta}_{a,b}^t$ as well as telescope-dependent amplitude errors g_a^t, g_b^t and phase errors ϕ_a^t, ϕ_b^t (EHTC, 2019a). To mitigate the impact of these amplitude and phase errors, derived data products called *closure quantities*, namely *closure phases* and *log closure amplitudes*, can be used to constrain inference (Blackburn et al., 2020):

$$\mathbf{y}_{t,(a,b,c)}^{\text{cp}} = \angle(V_{a,b}^t V_{b,c}^t V_{a,c}^t) \in \mathbb{R}, \quad \mathbf{y}_{t,(a,b,c,d)}^{\text{logca}} = \log \left(\frac{|V_{a,b}^t| |V_{c,d}^t|}{|V_{a,c}^t| |V_{b,d}^t|} \right) \in \mathbb{R}. \quad (6)$$

Here, \angle and $|\cdot|$ denote the complex angle and amplitude. Given a total of M telescopes, the number of closure phase measurements $\mathbf{y}_{t,(a,b,c)}^{\text{cp}}$ at time t is $\frac{(M-1)(M-2)}{2}$, and the number of log closure amplitude measurements $\mathbf{y}_{t,(a,b,c,d)}^{\text{logca}}$ is $\frac{M(M-3)}{2}$, after accounting for redundancy. Closure quantities are nonlinear transformations of the visibilities, making a forward model that uses them for black hole imaging non-convex. The inverse problem is further complicated by the need for super-resolution imaging beyond the intrinsic resolution of the Event Horizon Telescope (EHT) observations (i.e., maximum probed spatial frequency), as well as phase ambiguities, which can lead to multiple modes in the posterior distribution (Sun & Bouman, 2021; Sun et al., 2024). Another challenge of BHI is that measurement noise is non-additive due to the usage of the closure quantities.

Full waveform inversion Full waveform inversion (FWI) aims to infer subsurface physical properties (e.g. compressional and shear wave velocities) using both amplitude and phase information of recorded waveforms. Compared to traveltimes tomography based on the ray theory (Guo et al., 2015; Li et al., 2023), FWI can reveal more detailed geological structures. In this work, we consider the problem of recovering the compressional wave velocity $\mathbf{z} \in \mathbb{R}^n$ from the observed waveforms

$$\mathbf{y} = \mathbf{P}\mathbf{u} \in \mathbb{R}^m \quad \text{where} \quad \mathbf{u} = \mathbf{A}(\mathbf{m})^{-1}\mathbf{q}_s. \quad (7)$$

Here, $\mathbf{P} \in \{0, 1\}^{m \times n}$ is the sampling operator of the receivers at the free surface, $\mathbf{u} := \mathbf{u}(\mathbf{x}, t)$ is the pressure wavefield at location \mathbf{x} and time t , $\mathbf{m} := \frac{1}{z^2}$ is the square slowness, \mathbf{q}_s is the source,

and \mathbf{A} is the discretization matrix of the following acoustic wave equation that models seismic wave propagation in heterogeneous acoustic media

$$m \frac{d^2 \mathbf{u}(\mathbf{x}, t)}{dt^2} - \nabla^2 \mathbf{u}(\mathbf{x}, t) = \mathbf{q}_s \text{ in } \Omega, \text{ s.t. } \mathbf{u}(\cdot, 0) = \mathbf{0}, \left. \frac{d\mathbf{u}(\mathbf{x}, t)}{dt} \right|_{t=0} = \mathbf{0}, \mathbf{u}(\mathbf{x}, t) \Big|_{\partial\Omega} = \mathbf{0} \quad (8)$$

which can be discretized as $\mathbf{A}(\mathbf{m})\mathbf{u} = \mathbf{q}_s$. Since we only have observations at the free surface, this inverse problem ill-posed and leads to non-unique solutions. One of the major challenges for FWI is the prohibitive computational expense, especially for large problems, as it usually requires numerous calls to the forward modeling process, which is computationally expensive. Moreover, the conventional method for FWI, called the adjoint-state method, casts it as a local optimization problem (Virieux et al., 2017; Virieux & Operto, 2009). This means that a sufficiently accurate initial model is required, as the solution is only sought in its vicinity. FWI conventionally needs to start with a smoothed model derived from simpler ray-based methods (Liu et al., 2017; Maguire et al., 2022; Zhang et al., 2018a), which imposes a significantly strong prior. A more general method for FWI is highly desired to reduce reliance on initialization.

Navier-Stokes equation Navier-Stokes equation is a classic benchmarking problem from fluid dynamics (Iglesias et al., 2013). Its applications range from ocean dynamics to climate modeling where observations of the atmosphere are used to calibrate the initial condition for the downstream numerical forecasting. The forward model is given by the following 2D Navier-Stokes equation for a viscous, incompressible fluid in vorticity form on a torus.

$$\begin{aligned} \partial_t \mathbf{w}(\mathbf{x}, t) + \mathbf{u}(\mathbf{x}, t) \cdot \nabla \mathbf{w}(\mathbf{x}, t) &= \nu \Delta \mathbf{w}(\mathbf{x}, t) + f(\mathbf{x}), & \mathbf{x} \in (0, 2\pi)^2, t \in (0, T] \\ \nabla \cdot \mathbf{u}(\mathbf{x}, t) &= \mathbf{0}, & \mathbf{x} \in (0, 2\pi)^2, t \in [0, T] \\ \mathbf{w}(\mathbf{x}, 0) &= \mathbf{w}_0(\mathbf{x}), & \mathbf{x} \in (0, 2\pi)^2 \end{aligned} \quad (9)$$

where $\mathbf{u} \in C([0, T]; H_{\text{per}}^r((0, 2\pi)^2; \mathbb{R}^2))$ for any $r > 0$ is the velocity field, $\mathbf{w} = \nabla \times \mathbf{u}$ is the vorticity, $\mathbf{w}_0 \in L_{\text{per}}^2((0, 2\pi)^2; \mathbb{R})$ is the initial vorticity, $\nu \in \mathbb{R}_+$ is the viscosity coefficient, and $f \in L_{\text{per}}^2((0, 2\pi)^2; \mathbb{R})$ is the forcing function. The solution operator \mathcal{G} is defined as the operator mapping the vorticity from the initial vorticity to the vorticity at time T , i.e. $\mathcal{G} : \mathbf{w}_0 \rightarrow \mathbf{w}_T$. We consider the problem of recovering the initial vorticity field $\mathbf{z} := \mathbf{w}_0$ from the noisy partial observation \mathbf{y} of the vorticity field \mathbf{w}_T at time T given by

$$\mathbf{y} = \mathbf{P}\mathbf{L}(\mathbf{z}) + \mathbf{n}$$

where \mathbf{P} is the sampling operator, \mathbf{n} is the AWGN, and $\mathbf{L}(\cdot)$ is the discretized solution operator of (9). The Navier-Stokes equation (9) does not admit a closed-form solution and thus there is no closed-form gradient available for the solution operator. Moreover, obtaining an accurate numerical gradient via automatic differentiation through the numerical solver is challenging due to the extensive computation graph expanded after thousands of discrete time steps.

4 EXPERIMENTS

4.1 EXPERIMENTAL SETUP

Here we provide a brief summary of our experimental setup. More details about the inverse problems and their corresponding datasets can be found in Appendix A.2. Technical details of DM pretraining can be found in Appendix A.3.

Black hole imaging We leverage a dataset of General Relativistic MagnetoHydroDynamic (GRMHD) (Mizuno, 2022) simulated black hole images as our training data. The training set consists of 50,000 resized 64×64 images. Since this dataset is not publicly available, we generate synthetic images from a pre-trained diffusion model for both the validation and test datasets. Specifically, we use 5 sampled images for the validation set and 100 sampled images for the test set.

Full waveform inversion We adapt the CurveFaultB dataset introduced by (Deng et al., 2022), which presents the velocity maps that contain faults caused by shifted rock layers. We resize the original data to resolution 128×128 with bilinear interpolation and anti-aliasing. The training set consists of 50,000 velocity maps. The test and validation sets contain 10 and 1 velocity maps, respectively.

Linear inverse scattering We create a dataset of fluorescence microscopy images using the online simulator (Wiesner et al., 2019). The training set consists of 10,000 HL60 nucleus permittivity images. The test and validation sets contain 100 and 10 permittivity images, respectively. We curate the test and validation samples so that all test samples have less than 0.6 cosine similarities to those in the training set.

Compressed sensing MRI We use the multi-coil raw k -space data from the fastMRI knee dataset (Zbontar et al., 2018). We exclude the first and last 5 slices of each volume for training and validation as they do not contain much anatomical information and resize all images down to 320×320 following the preprocessing procedure of (Jalal et al., 2021). In total, we use 25,012 images for training, 6 images for hyperparameter search, and 94 images for testing.

Navier-Stokes We create a dataset of non-trivial initial vorticity fields by sampling from a Gaussian random field. Then we evolve Eq.9 for five time units. We use the Reynolds number to 200 and spatial resolution 128×128 . The training set consists of 10,000 samples. The test and validation sets contain 10 and 1 vorticity fields, respectively.

Pretraining of diffusion model priors For each inverse problem, we train a diffusion model on the training set using the pipeline from (Karras et al., 2022), and use the same checkpoint for all diffusion plug-and-play methods on each problem for a fair comparison.

4.2 EVALUATION METRICS

Accuracy metrics We use the Peak Signal-to-Noise Ratio (PSNR), Structure Similarity Index Measure (SSIM), as the generic ways to quantify recovery of the true source. For all the problems except for black hole imaging, we use the L2 error $\|G(\hat{z}) - \mathbf{y}\|_2$ to measure the consistency with the observation \mathbf{y} . For black hole imaging, the closure quantities are invariant under translation, and so we measure the best fit under any shift alignment. We also assess the Blur PSNR, where images are blurred to match the target resolution of the telescope. We evaluate data misfit via the χ^2 statistic on two closure quantities: the closure phase (χ_{cp}^2) and the log closure amplitude (χ_{logca}^2). A χ^2 value close to 1 indicates better data fitting. To facilitate a comparison between underfitting ($\chi^2 > 1$) and overfitting ($\chi^2 < 1$), we report a unified metric defined as

$$\tilde{\chi}^2 = \chi^2 \cdot \mathbb{1}\{\chi^2 \geq 1\} + \frac{1}{\chi^2} \cdot \mathbb{1}\{\chi^2 < 1\}. \quad (10)$$

For FWI and Navier-Stokes experiments, we also use the relative ℓ_2 error $\|\hat{z} - z\|_2 / \|z\|_2$ as it is a commonly used primary accuracy metric in PDE problems (Iglesias et al., 2013).

Efficiency metrics We define a set of efficiency metrics in Table 9 to evaluate the computational complexity of inverse algorithms more thoroughly. These metrics fall into two categories: (1) total metrics that measure the overall computational cost; (2) sequential metrics that help identify bottlenecks where forward model or diffusion model queries cannot be parallelized.

Ranking score To assess the relative ranking of different PnP diffusion models across various problems, we define the following ranking score for each problem. Given a set of accuracy or efficiency metrics $\{h_k\}_{k=1}^K$, we rank the algorithms according to each individual metric. Suppose algorithm l has the rank $R_k(l)$ out of L algorithms under the metric k . Its ranking score on this metric is given by:

$$\text{score}_k(l) = 100 \times (L - R_k(l) + 1) / L. \quad (11)$$

For each problem, we calculate the average ranking score to assess overall performance:

$$\text{score}^{\text{problem}}(l) = \frac{1}{K} \sum_{k=1}^K \text{score}_k(l). \quad (12)$$

4.3 MAIN FINDINGS

The full experimental results for each problem are provided in Appendix A.1 as tables. Below, we highlight some key insights distilled from these results.

378
379
380
381
382
383
384
385
386
387
388
389
390
391
392
393
394
395
396
397
398
399
400
401
402
403
404
405
406
407
408
409
410
411
412
413
414
415
416
417
418
419
420
421
422
423
424
425
426
427
428
429
430
431

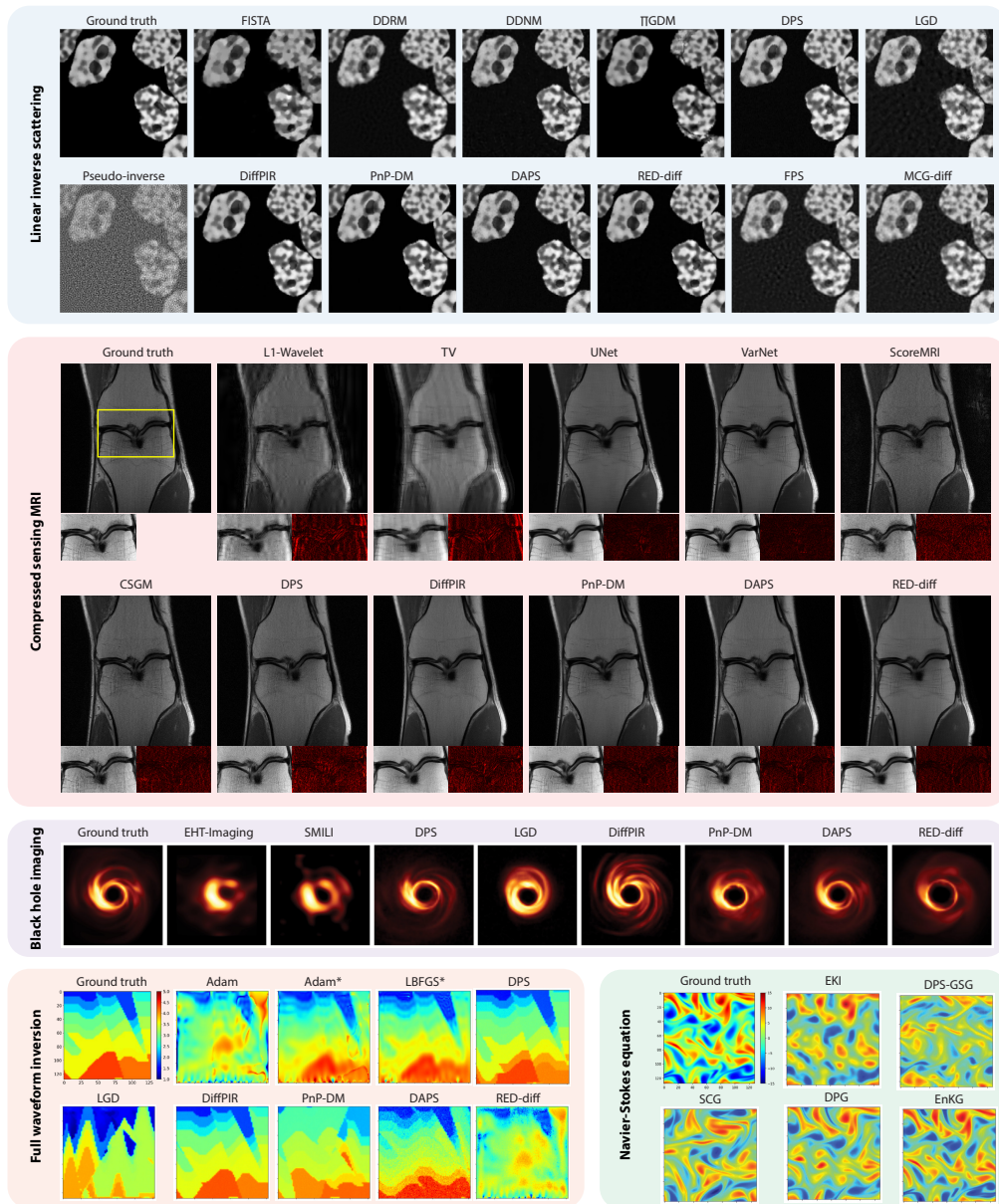


Figure 2: Visual examples for each problem. In the linear inverse scattering task, PnP diffusion prior methods can generate shaper images than the traditional baseline FISTA. For black hole imaging, the baselines are blurrier than plug-in-plug diffusion prior methods. Full waveform inversion: Adam* and LBFGS* are initialized from Gaussian blurred ground truth. With random or constant initialization, these optimization methods simply fail. Navier-Stokes equation: PnP diffusion prior methods capture more rich flow feature than the conventional baseline.

How do PnP diffusion prior methods work compared to conventional baselines? Our primary finding is that, given a suitable dataset for training a DM prior, PnP diffusion prior methods generally outperform conventional baselines. This is evident in Figure 1, where the PnP diffusion prior methods generally lie higher along the vertical axis. This finding is as expected given that the baselines do not incorporate such strong prior information.

However, if the classic optimization baselines are initialized well, then they sometimes outperform PnP diffusion model methods, most of which cannot naturally incorporate an initialization beyond white noise. For example, in FWI, PnP diffusion prior methods clearly outperform the classic baseline methods if the baselines are initialized randomly or from a constant. But if initialized with a

good guess (e.g., a heavily blurred ground truth image), they consistently outperform the current PnP diffusion prior methods. That being said, the fact that PnP diffusion prior methods rely much less on initialization than the traditional optimization methods is already an intriguing property. See qualitative comparison in Figure 1 and quantitative comparison in Table 7.

How do PnP diffusion prior methods compare with each other? In the problems where the forward model has a closed-form expression, methods that require more gradient queries, such as DAPS and PnP-DM, tend to be more accurate. However, since they have more queries to the forward model, they are also more expensive, as shown in Figure 1. Additionally, these methods require more careful tuning as they usually have larger hyperparameter spaces, as shown in Table 11¹.

In the problems where the forward model has no closed-form expression, particularly a forward model defined by a PDE system and implemented as a numerical PDE solver, this trend does not hold. In fact, DAPS and PnP-DM perform poorly, as shown in Figure 1 and Table 7. These methods also demonstrate an increased level of numerical instability and sensitivity to hyperparameters, as shown in Figure 3: minor adjustments in step size can lead to either unconditional generation results that ignore measurements (with slightly smaller steps) or complete failure (with slightly larger steps). This performance degradation stems from a critical limitation in many current PnP diffusion prior algorithms: they do not account for stability conditions required to query a forward model. For example, in the FWI and Navier-Stokes equation, the input of the forward model must satisfy the Courant-Friedrichs-Lewy (CFL) condition (Courant et al., 1967) to produce stable solutions. This issue is particularly pronounced for methods like DAPS and PnP-DM, which incorporate Langevin Monte Carlo (LMC) as an inner loop as LMC introduces additional Gaussian noise at each step, further exacerbating instability compared to other PnP diffusion prior methods.

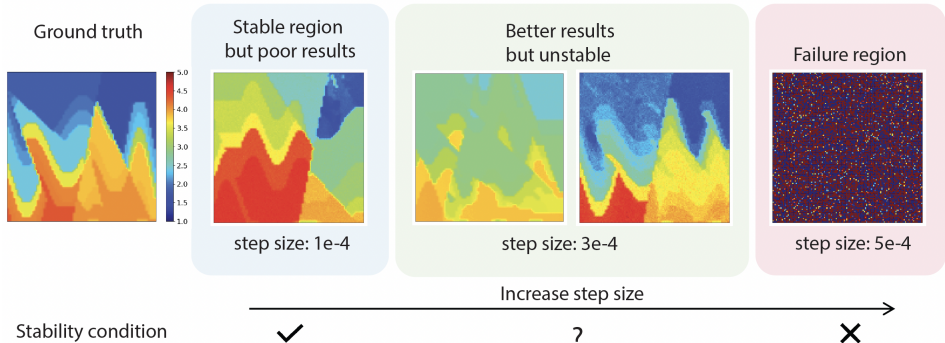


Figure 3: Illustration of the failures of PnP diffusion models (DAPS as an example) on full waveform inversion. With a small learning rate, DAPS is numerically stable but does not solve the inverse problem effectively. With a slightly larger learning rate, DAPS produces a noisy velocity map that breaks the stability condition of the PDE solver, resulting in a complete failure.

How does the performance vary with different levels of measurement sparsity? As measurement sparsity increases, making the inverse problem more ill-posed, we observe an increasingly wide performance gap between PnP diffusion prior methods and baselines. Figure 4 illustrates this trend across three problems, showing that the average performance gain of top PnP diffusion prior methods over baselines grows with increasing measurement sparsity.

How well do PnP diffusion prior methods deal with different forward models? For linear inverse problems, our results demonstrate that PnP diffusion prior methods can effectively deal with varying forward models without the need for parameter tuning. To validate this, we conduct a controlled experiment in CS-MRI, where we maintain a consistent measurement sparsity while altering the subsampling pattern (from vertical to horizontal lines). We assess the average performance variation across three method categories: traditional baselines, end-to-end approaches, and PnP diffusion prior methods. The average absolute performance change for PnP diffusion prior methods is 0.48 (PSNR) and 0.016 (SSIM), comparable to the traditional baseline methods at 1.62 (PSNR) and

¹Note that tuning the hyperparameters of PnP diffusion prior approaches is still much more efficient than retraining a neural network that is typically required for end-to-end approaches.

486
487
488
489
490
491
492
493
494
495
496
497
498
499
500
501
502
503
504
505
506
507
508
509
510
511
512
513
514
515
516
517
518
519
520
521
522
523
524
525
526
527
528
529
530
531
532
533
534
535
536
537
538
539

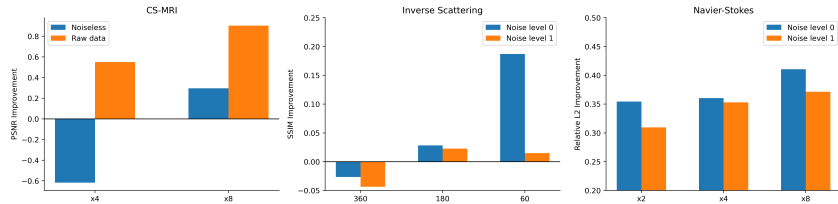


Figure 4: Relative performance of plug-and-play diffusion prior methods compared with traditional baselines under different levels of measurement sparsity on different tasks. Metrics are averaged over multiple PnP diffusion prior methods. The performance difference increases in general as the measurement becomes sparser.

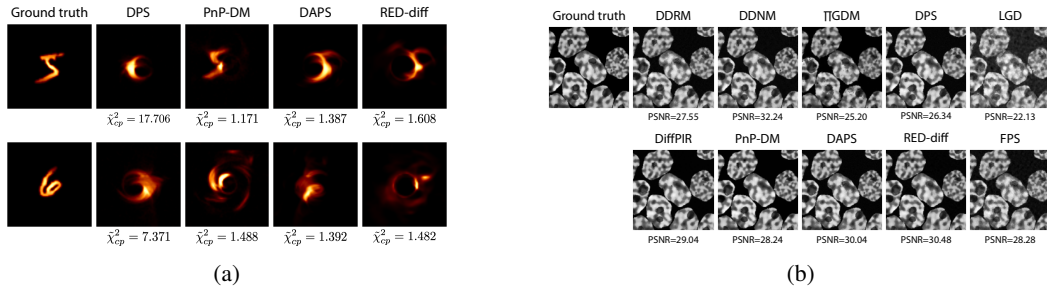


Figure 5: PnP diffusion prior methods on out-of-distribution test samples. (a) Black-hole imaging problem on digits inputs; and (b) inverse scattering on sources that contain 9 cells, while the prior model is trained on images with 1 to 6 cells.

0.027 (SSIM), but significantly smaller than the end-to-end methods, which exhibit changes of 9.58 (PSNR) and 0.21 (SSIM). These findings indicate that PnP diffusion prior methods are more robust than both baseline and end-to-end methods when handling different forward models.²

How well do PnP diffusion prior methods handle out-of-distribution sources? In general, if the unknown source falls outside the diffusion prior distribution, PnP diffusion prior methods tend to generate solutions that are biased toward the prior. As illustrated in Figure 5a, most solutions produced by PnP diffusion prior methods exhibit a black hole ring feature characteristic of the diffusion prior. This suggests that while PnP diffusion prior approaches are flexible in capturing high-dimensional priors, they are limited in their ability to reliably recover “surprising” sources that lie outside the support of the diffusion prior distribution. However, when the unknown source is close to the diffusion prior distribution, PnP diffusion prior methods can recover it effectively, as demonstrated in Figure 5b.

5 DISCUSSION

Finally, we close with a brief discussion of some research opportunities in PnP diffusion prior to solving inverse problems. The first research opportunity is related to our previous findings that the current PnP diffusion prior methods do not account for stability conditions required to query a forward model, which results in poor performance. However, many scientific inverse problems are based on PDE systems that are implemented as numerical solvers, which will produce incorrect or unreliable results if the input does not satisfy the stability conditions. Therefore, developing new algorithms that ensure the stability condition for PDE will be of great interest and value to solving scientific inverse problems. Another exciting direction is about improving the inference speed of PnP diffusion prior to methods. As shown in Figure 1, almost all the PnP diffusion prior methods are less computationally efficient than the conventional baselines. We believe there is a big headroom for efficiency improvement of PnP diffusion prior methods.

²For end-to-end approaches, this is considered as an out-of-distribution test.

REFERENCES

- 540
541
542 Hemant Aggarwal, Merry Mani, and Mathews Jacob. Modl: Model based deep learning architecture
543 for inverse problems. *IEEE Transactions on Medical Imaging*, PP, 12 2017. doi: 10.1109/TMI.
544 2018.2865356.
- 545 Kazunori Akiyama, Shiro Ikeda, Mollie Pleau, Vincent L Fish, Fumie Tazaki, Kazuki Kuramochi,
546 Avery E Broderick, Jason Dexter, Monika Mościbrodzka, Michael Gowanlock, et al. Superreso-
547 lution full-polarimetric imaging for radio interferometry with sparse modeling. *The Astronomical*
548 *Journal*, 153(4):159, 2017a.
- 549 Kazunori Akiyama, Kazuki Kuramochi, Shiro Ikeda, Vincent L Fish, Fumie Tazaki, Mareki Honma,
550 Sheperd S Doleman, Avery E Broderick, Jason Dexter, Monika Mościbrodzka, et al. Imaging
551 the schwarzschild-radius-scale structure of m87 with the event horizon telescope using sparse
552 modeling. *The Astrophysical Journal*, 838(1):1, 2017b.
- 553 Kazunori Akiyama, Fumie Tazaki, Kotaro Moriyama, Ilje Cho, Shiro Ikeda, Mahito Sasada, Hiroki
554 Okino, and Mareki Honma. Smili: Sparse modeling imaging library for interferometry. *Astro-*
555 *physics Source Code Library*, pp. ascl-1904, 2019.
- 556
557 Albert S Berahas, Liyuan Cao, Krzysztof Choromanski, and Katya Scheinberg. A theoretical and
558 empirical comparison of gradient approximations in derivative-free optimization. *Foundations of*
559 *Computational Mathematics*, 22(2):507–560, 2022.
- 560
561 Lindy Blackburn, Dominic W. Pesce, Michael D. Johnson, Maciek Wielgus, Andrew A. Chael,
562 Pierre Christian, and Sheperd S. Doleman. Closure statistics in interferometric data. *The As-*
563 *trophysical Journal*, 894(1):31, may 2020. doi: 10.3847/1538-4357/ab8469. URL <https://dx.doi.org/10.3847/1538-4357/ab8469>.
- 564
565 C. Bouman and K. Sauer. A generalized gaussian image model for edge-preserving map estimation.
566 *IEEE Transactions on Image Processing*, 2(3):296–310, 1993. doi: 10.1109/83.236536.
- 567
568 Benjamin Boys, Mark Girolami, Jakiw Pidstrigach, Sebastian Reich, Alan Mosca, and O. Deniz
569 Akyildiz. Tweedie moment projected diffusions for inverse problems, 2023.
- 570
571 D. J. Brady, K. Choi, D. L. Marks, R. Horisaki, and S. Lim. Compressive holography. *Opt. Express*,
17(15):13040–13049, 2009.
- 572
573 M. M. Bronstein, A. M. Bronstein, M. Zibulevsky, and H. Azhari. Reconstruction in diffraction
574 ultrasound tomography using nonuniform FFT. *IEEE Trans. Med. Imag.*, 21(11):1395–1401,
575 November 2002.
- 576
577 Ruiming Cao, Nikita S Divekar, James K Nuñez, Srigokul Upadhyayula, and Laura Waller. Neural
space–time model for dynamic multi-shot imaging. *Nature Methods*, pp. 1–6, 2024.
- 578
579 Gabriel Cardoso, Yazid Janati el idrissi, Sylvain Le Corff, and Eric Moulines. Monte carlo guided
580 denoising diffusion models for bayesian linear inverse problems. In *The Twelfth International*
581 *Conference on Learning Representations*, 2024. URL <https://openreview.net/forum?id=nHESwXvzWK>.
- 582
583 James A Carton and Benjamin S Giese. A reanalysis of ocean climate using simple ocean data
584 assimilation (soda). *Monthly weather review*, 136(8):2999–3017, 2008.
- 585
586 Andrew Chael, Katie Bouman, Michael Johnson, Maciek Wielgus, Lindy Blackburn, Chi-Kwan
587 Chan, Joseph Rachid Farah, Daniel Palumbo, and Dominic Pesce. eht-imaging: v1. 1.0: Imaging
interferometric data with regularized maximum likelihood. *Zenodo*, 2019.
- 588
589 Andrew A Chael, Michael D Johnson, Ramesh Narayan, Sheperd S Doleman, John FC Wardle, and
590 Katherine L Bouman. High-resolution linear polarimetric imaging for the event horizon telescope.
591 *The Astrophysical Journal*, 829(1):11, 2016.
- 592
593 Andrew A Chael, Michael D Johnson, Katherine L Bouman, Lindy L Blackburn, Kazunori
Akiyama, and Ramesh Narayan. Interferometric imaging directly with closure phases and closure
amplitudes. *The Astrophysical Journal*, 857(1):23, 2018.

- 594 Michael Chen, David Ren, Hsiou-Yuan Liu, Shwetadwip Chowdhury, and Laura Waller. Multi-layer
595 born multiple-scattering model for 3d phase microscopy. *Optica*, 7(5):394–403, 2020.
596
- 597 Yongxin Chen, Sinho Chewi, Adil Salim, and Andre Wibisono. Improved analysis for a proximal
598 algorithm for sampling, 2022. URL <https://arxiv.org/abs/2202.06386>.
- 599 Cheng Chi, Siyuan Feng, Yilun Du, Zhenjia Xu, Eric Cousineau, Benjamin Burchfiel, and Shu-
600 ran Song. Diffusion policy: Visuomotor policy learning via action diffusion. *arXiv preprint*
601 *arXiv:2303.04137*, 2023.
- 602 W. Choi, C. Fang-Yen, K. Badizadegan, S. Oh, N. Lue, R. R. Dasari, and M. S. Feld. Tomographic
603 phase microscopy. *Nat. Methods*, 4(9):717–719, September 2007.
604
- 605 Hyungjin Chung and Jong Chul Ye. Score-based diffusion models for accelerated mri. *Medical*
606 *Image Analysis*, 80:102479, 05 2022. doi: 10.1016/j.media.2022.102479.
- 607 Hyungjin Chung, Jeongsol Kim, Michael Thompson Mccann, Marc Louis Klasky, and Jong Chul
608 Ye. Diffusion posterior sampling for general noisy inverse problems. In *The Eleventh Interna-*
609 *tional Conference on Learning Representations*, 2023. URL [https://openreview.net/](https://openreview.net/forum?id=OnD9zGAGT0k)
610 [forum?id=OnD9zGAGT0k](https://openreview.net/forum?id=OnD9zGAGT0k).
- 611
- 612 BG Clark. An efficient implementation of the algorithm ‘clean’. *Astronomy and Astrophysics*, vol.
613 89, no. 3, Sept. 1980, p. 377, 378., 89:377, 1980.
- 614 Robert Clayton and Björn Engquist. Absorbing boundary conditions for acoustic and elastic wave
615 equations. *Bulletin of the seismological society of America*, 67(6):1529–1540, 1977.
- 616
- 617 Richard Courant, Kurt Friedrichs, and Hans Lewy. On the partial difference equations of mathemat-
618 ical physics. *IBM journal of Research and Development*, 11(2):215–234, 1967.
- 619 Chengyuan Deng, Shihang Feng, Hanchen Wang, Xitong Zhang, Peng Jin, Yinan Feng, Qili Zeng,
620 Yinpeng Chen, and Youzuo Lin. Openfwi: Large-scale multi-structural benchmark datasets for
621 full waveform inversion. *Advances in Neural Information Processing Systems*, 35:6007–6020,
622 2022.
- 623 A. J. Devaney. Inverse-scattering theory within the Rytov approximation. *Opt. Lett.*, 6(8):374–376,
624 August 1981.
- 625
- 626 Prafulla Dhariwal and Alexander Nichol. Diffusion models beat gans on image synthesis. *Advances*
627 *in neural information processing systems*, 34:8780–8794, 2021.
- 628 Noe Dia, MJ Yantovski-Barth, Alexandre Adam, Micah Bowles, Pablo Lemos, Anna MM Scaife,
629 Yashar Hezaveh, and Laurence Perreault-Levasseur. Bayesian imaging for radio interferometry
630 with score-based priors. *arXiv preprint arXiv:2311.18012*, 2023.
- 631
- 632 Zehao Dou and Yang Song. Diffusion posterior sampling for linear inverse problem solving: A
633 filtering perspective. In *The Twelfth International Conference on Learning Representations*, 2024.
- 634 Event Horizon Telescope Collaboration EHTC. First sagittarius a* event horizon telescope results.
635 iii. imaging of the galactic center supermassive black hole. *The Astrophysical Journal Letters*,
636 930(2):L14, may 2022. doi: 10.3847/2041-8213/ac6429. URL [https://dx.doi.org/10.](https://dx.doi.org/10.3847/2041-8213/ac6429)
637 [3847/2041-8213/ac6429](https://dx.doi.org/10.3847/2041-8213/ac6429).
- 638 The Event Horizon Telescope Collaboration EHTC. First m87 event horizon telescope results. iii.
639 data processing and calibration. *The Astrophysical Journal Letters*, 875(1):L3, apr 2019a. doi: 10.
640 [3847/2041-8213/ab0c57](https://dx.doi.org/10.3847/2041-8213/ab0c57). URL <https://dx.doi.org/10.3847/2041-8213/ab0c57>.
- 641
- 642 The Event Horizon Telescope Collaboration EHTC. First m87 event horizon telescope results.
643 iv. imaging the central supermassive black hole. *The Astrophysical Journal Letters*, 875(1):
644 L4, apr 2019b. doi: 10.3847/2041-8213/ab0e85. URL [https://dx.doi.org/10.3847/](https://dx.doi.org/10.3847/2041-8213/ab0e85)
645 [2041-8213/ab0e85](https://dx.doi.org/10.3847/2041-8213/ab0e85).
- 646 The Event Horizon Telescope Collaboration EHTC. The persistent shadow of the supermassive
647 black hole of m 87-i. observations, calibration, imaging, and analysis. *Astronomy & Astrophysics*,
681:A79, 2024.

- 648 Berthy Feng and Katherine Bouman. Variational bayesian imaging with an efficient surrogate score-
649 based prior. *Transactions on Machine Learning Research*, 2024. ISSN 2835-8856. URL <https://openreview.net/forum?id=db2pFKVcm1>.
650
651
- 652 Berthy T Feng, Jamie Smith, Michael Rubinstein, Huiwen Chang, Katherine L Bouman, and
653 William T Freeman. Score-based diffusion models as principled priors for inverse imaging. In
654 *Proceedings of the IEEE/CVF International Conference on Computer Vision*, pp. 10520–10531,
655 2023.
- 656 Berthy T Feng, Katherine L Bouman, and William T Freeman. Event-horizon-scale imag-
657 ing of m87* under different assumptions via deep generative image priors. *arXiv preprint*
658 *arXiv:2406.02785*, 2024.
659
- 660 Cong Fu, Keqiang Yan, Limei Wang, Wing Yee Au, Michael Curtis McThrow, Tao Komikado, Koji
661 Maruhashi, Kanji Uchino, Xiaoning Qian, and Shuiwang Ji. A latent diffusion model for protein
662 structure generation. In *Learning on Graphs Conference*, pp. 29–1. PMLR, 2024.
- 663 Alfredo Garbuno-Inigo, Franca Hoffmann, Wuchen Li, and Andrew M Stuart. Interacting langevin
664 diffusions: Gradient structure and ensemble kalman sampler. *SIAM Journal on Applied Dynamical*
665 *Systems*, 19(1):412–441, 2020.
666
- 667 Zhen Guo, Y John Chen, Jieyuan Ning, Yongge Feng, Stephen P Grand, Fenglin Niu, Hitoshi
668 Kawakatsu, Satoru Tanaka, Masayuki Obayashi, and James Ni. High resolution 3-d crustal
669 structure beneath ne china from joint inversion of ambient noise and receiver functions using
670 necessarray data. *Earth and Planetary Science Letters*, 416:1–11, 2015.
- 671 Jacques Hadamard. *Lectures on Cauchy’s problem in linear partial differential equations*. Courier
672 Corporation, 2014.
673
- 674 Kerstin Hammernik, Teresa Klatzer, Erich Kobler, Michael P. Recht, Daniel K. Sodickson, Thomas
675 Pock, and Florian Knoll. Learning a variational network for reconstruction of accelerated MRI
676 data. *CoRR*, abs/1704.00447, 2017.
- 677 Yinnian He and Weiwei Sun. Stability and convergence of the crank–nicolson/adams–bashforth
678 scheme for the time-dependent navier–stokes equations. *SIAM Journal on Numerical Analysis*,
679 45(2):837–869, 2007.
680
- 681 JA Högbom. Aperture synthesis with a non-regular distribution of interferometer baselines. *Astron-*
682 *omy and Astrophysics Supplement, Vol. 15, p. 417*, 15:417, 1974.
- 683 Yue Huang, John W. Paisley, Qin Lin, Xinghao Ding, Xueyang Fu, and Xiao-Ping (Steven) Zhang.
684 Bayesian nonparametric dictionary learning for compressed sensing MRI. *IEEE Trans. Image*
685 *Process.*, 23(12):5007–5019, 2014.
686
- 687 Yujia Huang, Adishree Ghatare, Yuanzhe Liu, Ziniu Hu, Qinsheng Zhang, Chandramouli
688 Shama Sastry, Siddharth Gururani, Sageev Oore, and Yisong Yue. Symbolic music generation
689 with non-differentiable rule guided diffusion. In Ruslan Salakhutdinov, Zico Kolter, Kather-
690 ine Heller, Adrian Weller, Nuria Oliver, Jonathan Scarlett, and Felix Berkenkamp (eds.), *Pro-*
691 *ceedings of the 41st International Conference on Machine Learning*, volume 235 of *Proceed-*
692 *ings of Machine Learning Research*, pp. 19772–19797. PMLR, 21–27 Jul 2024. URL <https://proceedings.mlr.press/v235/huang24g.html>.
693
- 694 Chang Min Hyun, Hwa Pyung Kim, Sung Min Lee, Sungchul Lee, and Jin Keun Seo. Deep learning
695 for undersampled MRI reconstruction. *CoRR*, abs/1709.02576, 2017.
- 696 Marco A Iglesias, Kody JH Law, and Andrew M Stuart. Ensemble kalman methods for inverse
697 problems. *Inverse Problems*, 29(4):045001, 2013.
698
- 699 Ajil Jalal, Marius Arvinte, Giannis Daras, Eric Price, Alex Dimakis, and Jonathan Tamir. Robust
700 compressed sensing MRI with deep generative priors. In A. Beygelzimer, Y. Dauphin, P. Liang,
701 and J. Wortman Vaughan (eds.), *Advances in Neural Information Processing Systems*, 2021. URL
<https://openreview.net/forum?id=wHoIjrT6MMb>.

- 702 Avinash C Kak and Malcolm Slaney. *Principles of computerized tomographic imaging*. SIAM,
703 2001.
- 704
- 705 Ulugbek S Kamilov, Ioannis N Papadopoulos, Morteza H Shoreh, Alexandre Goy, Cedric Vonesch,
706 Michael Unser, and Demetri Psaltis. Learning approach to optical tomography. *Optica*, 2(6):
707 517–522, 2015.
- 708 Tero Karras, Miika Aittala, Timo Aila, and Samuli Laine. Elucidating the design space of diffusion-
709 based generative models. *Advances in Neural Information Processing Systems*, 35:26565–26577,
710 2022.
- 711 Bahjat Kawar, Michael Elad, Stefano Ermon, and Jiaming Song. Denoising diffusion restoration
712 models. *Advances in Neural Information Processing Systems*, 35:23593–23606, 2022.
- 713
- 714 Diederik P Kingma. Adam: A method for stochastic optimization. *arXiv preprint arXiv:1412.6980*,
715 2014.
- 716 Nikola B Kovachki and Andrew M Stuart. Ensemble kalman inversion: a derivative-free technique
717 for machine learning tasks. *Inverse Problems*, 35(9):095005, 2019.
- 718
- 719 Dongwook Lee, Jae Jun Yoo, and Jong Chul Ye. Deep residual learning for compressed sensing
720 MRI. In *14th IEEE International Symposium on Biomedical Imaging, ISBI 2017, Melbourne,*
721 *Australia, April 18-21, 2017*, pp. 15–18. IEEE, 2017.
- 722
- 723 Yin Tat Lee, Ruoqi Shen, and Kevin Tian. Structured logconcave sampling with a restricted gaussian
724 oracle, 2021. URL <https://arxiv.org/abs/2010.03106>.
- 725 Lianlin Li, Long Gang Wang, Fernando L Teixeira, Che Liu, Arye Nehorai, and Tie Jun Cui. Deepn-
726 nis: Deep neural network for nonlinear electromagnetic inverse scattering. *IEEE Transactions on*
727 *Antennas and Propagation*, 67(3):1819–1825, 2018a.
- 728 Lisha Li, Kevin Jamieson, Giulia DeSalvo, Afshin Rostamizadeh, and Amee Talwalkar. Hyperband:
729 A novel bandit-based approach to hyperparameter optimization. *Journal of Machine Learning*
730 *Research*, 18(185):1–52, 2018b.
- 731
- 732 Xiang Li, Soo Min Kwon, Ismail R. Alkhouri, Saiprasad Ravishankar, and Qing Qu. Decoupled data
733 consistency with diffusion purification for image restoration, 2024. URL <https://arxiv.org/abs/2403.06054>.
- 734
- 735 Yida Li, Valeria Villa, Robert W Clayton, and Patricia Persaud. Shear wave velocities in the san
736 gabriel and san bernardino basins, california. *Journal of Geophysical Research: Solid Earth*, 128
737 (7):e2023JB026488, 2023.
- 738
- 739 Yunzhe Li, Yujia Xue, and Lei Tian. Deep speckle correlation: a deep learning approach toward
740 scalable imaging through scattering media. *Optica*, 5(10):1181–1190, 2018c.
- 741 H.-Y. Liu, D. Liu, H. Mansour, P. T. Boufounos, L. Waller, and U. S. Kamilov. SEAGLE: Sparsity-
742 driven image reconstruction under multiple scattering. *IEEE Trans. Comput. Imaging*, 4(1):73–86,
743 March 2018.
- 744
- 745 Jiaming Liu, Yu Sun, Cihat Eldeniz, Weijie Gan, Hongyu An, and Ulugbek S. Kamilov. RARE:
746 image reconstruction using deep priors learned without groundtruth. *IEEE J. Sel. Top. Signal*
747 *Process.*, 14(6):1088–1099, 2020.
- 748 Jiaming Liu, Yu Sun, Weijie Gan, Xiaojian Xu, Brendt Wohlberg, and Ulugbek S. Kamilov. Sgd-net:
749 Efficient model-based deep learning with theoretical guarantees. *CoRR*, abs/2101.09379, 2021.
- 750 Renhao Liu, Yu Sun, Jiabei Zhu, Lei Tian, and Ulugbek S Kamilov. Recovery of continuous 3d
751 refractive index maps from discrete intensity-only measurements using neural fields. *Nature Ma-*
752 *chine Intelligence*, 4(9):781–791, 2022.
- 753
- 754 Yaning Liu, Fenglin Niu, Min Chen, and Wencai Yang. 3-d crustal and uppermost mantle structure
755 beneath ne china revealed by ambient noise adjoint tomography. *Earth and Planetary Science*
Letters, 461:20–29, 2017.

- 756 M. Louboutin, M. Lange, F. Luporini, N. Kukreja, P. A. Witte, F. J. Herrmann, P. Velesko, and G. J.
757 Gorman. Devito (v3.1.0): an embedded domain-specific language for finite differences and geo-
758 physical exploration. *Geoscientific Model Development*, 12(3):1165–1187, 2019. doi: 10.5194/
759 gmd-12-1165-2019. URL <https://www.geosci-model-dev.net/12/1165/2019/>.
760
- 761 Guanxiong Luo, Na Zhao, Wenhao Jiang, Edward S. Hui, and Peng Cao. Mri reconstruction using
762 deep bayesian estimation. *Magnetic Resonance in Medicine*, 84:2246 – 2261, 2019. URL
763 <https://api.semanticscholar.org/CorpusID:215727630>.
- 764 Guanxiong Luo, Moritz Blumenthal, Martin Heide, and Martin Uecker. Bayesian mri re-
765 construction with joint uncertainty estimation using diffusion models. *Magnetic Reso-
766 nance in Medicine*, 90:295 – 311, 2022. URL [https://api.semanticscholar.org/
767 CorpusID:256697667](https://api.semanticscholar.org/CorpusID:256697667).
- 768 Yanchen Luo, Junfeng Fang, Sihang Li, Zhiyuan Liu, Jiancan Wu, An Zhang, Wenjie Du, and Xiang
769 Wang. Text-guided small molecule generation via diffusion model. *iScience*, 2024.
770
- 771 M. Lustig, D. L. Donoho, J. M. Santos, and J. M. Pauly. Compressed sensing MRI. *IEEE Signal
772 Processing Magazine*, 25(2):72–82, 2008. doi: 10.1109/MSP.2007.914728.
773
- 774 Michael Lustig, David Donoho, and John Pauly. Sparse mri: The application of compressed sensing
775 for rapid mr imaging. *Magnetic resonance in medicine : official journal of the Society of Magnetic
776 Resonance in Medicine / Society of Magnetic Resonance in Medicine*, 58:1182–95, 12 2007. doi:
777 10.1002/mrm.21391.
- 778 Shiqian Ma, Wotao Yin, Yin Zhang, and A. Chakraborty. An efficient algorithm for compressed mr
779 imaging using total variation and wavelets. In *2008 IEEE Conference on Computer Vision and
780 Pattern Recognition*, pp. 1–8, 2008. doi: 10.1109/CVPR.2008.4587391.
- 781 Y. Ma, H. Mansour, D. Liu, P. T. Boufounos, and U. S. Kamilov. Accelerated image reconstruction
782 for nonlinear diffractive imaging. In *Proc. IEEE Int. Conf. Acoustics, Speech and Signal Process.
783 (ICASSP 2018)*, Calgary, Canada, April 15–20, 2018. arXiv:1708.01663 [cs.CV].
784
- 785 Ross Maguire, Brandon Schmandt, Jiaqi Li, Chengxin Jiang, Guoliang Li, Justin Wilgus, and Min
786 Chen. Magma accumulation at depths of prior rhyolite storage beneath yellowstone caldera.
787 *Science*, 378(6623):1001–1004, 2022.
788
- 789 Morteza Mardani, Jiaming Song, Jan Kautz, and Arash Vahdat. A variational perspective on solving
790 inverse problems with diffusion models. *arXiv preprint arXiv:2305.04391*, 2023.
- 791 Morteza Mardani, Jiaming Song, Jan Kautz, and Arash Vahdat. A variational perspective on solving
792 inverse problems with diffusion models. In *The Twelfth International Conference on Learning
793 Representations*, 2024. URL <https://openreview.net/forum?id=1Y04EE3SPB>.
794
- 795 Yosuke Mizuno. Grmhd simulations and modeling for jet formation and acceleration region in
796 agns. *Universe*, 8(2):85, January 2022. ISSN 2218-1997. doi: 10.3390/universe8020085. URL
797 <http://dx.doi.org/10.3390/universe8020085>.
- 798 R-E Plessix. A review of the adjoint-state method for computing the gradient of a functional with
799 geophysical applications. *Geophysical Journal International*, 167(2):495–503, 2006.
800
- 801 Oliver Porth, Koushik Chatterjee, Ramesh Narayan, Charles F Gammie, Yosuke Mizuno, Peter
802 Anninos, John G Baker, Matteo Bugli, Chi-kwan Chan, Jordy Davelaar, et al. The event horizon
803 general relativistic magnetohydrodynamic code comparison project. *The Astrophysical Journal
804 Supplement Series*, 243(2):26, 2019.
- 805 Tran Minh Quan, Thanh Nguyen-Duc, and Won-Ki Jeong. Compressed sensing MRI reconstruction
806 using a generative adversarial network with a cyclic loss. *IEEE Trans. Medical Imaging*, 37(6):
807 1488–1497, 2018.
808
- 809 Saiprasad Ravishankar and Yoram Bresler. MR image reconstruction from highly undersampled
k-space data by dictionary learning. *IEEE Trans. Medical Imaging*, 30(5):1028–1041, 2011.

- 810 Robin Rombach, Andreas Blattmann, Dominik Lorenz, Patrick Esser, and Björn Ommer. High-
811 resolution image synthesis with latent diffusion models. In *Proceedings of the IEEE/CVF confer-*
812 *ence on computer vision and pattern recognition*, pp. 10684–10695, 2022.
- 813 Litu Rout, Negin Raoof, Giannis Daras, Constantine Caramanis, Alex Dimakis, and Sanjay Shakkot-
814 tai. Solving linear inverse problems provably via posterior sampling with latent diffusion mod-
815 els. In *Thirty-seventh Conference on Neural Information Processing Systems*, 2023. URL
816 <https://openreview.net/forum?id=XKBFdYwfRo>.
- 817 Jo Schlemper, Jose Caballero, Joseph V. Hajnal, Anthony N. Price, and Daniel Rueckert. A deep
818 cascade of convolutional neural networks for dynamic MR image reconstruction. *IEEE Trans.*
819 *Medical Imaging*, 37(2):491–503, 2018.
- 820 Martin Shepherd. Difmap: Synthesis imaging of visibility data. *Astrophysics Source Code Library*,
821 pp. ascl-1103, 2011.
- 822 MC Shepherd. Difmap: an interactive program for synthesis imaging. In *Astronomical Data Anal-*
823 *ysis Software and Systems VI*, volume 125, pp. 77, 1997.
- 824 Jascha Sohl-Dickstein, Eric Weiss, Niru Maheswaranathan, and Surya Ganguli. Deep unsupervised
825 learning using nonequilibrium thermodynamics. In *International conference on machine learn-*
826 *ing*, pp. 2256–2265. PMLR, 2015.
- 827 Bowen Song, Soo Min Kwon, Zecheng Zhang, Xinyu Hu, Qing Qu, and Liyue Shen. Solving
828 inverse problems with latent diffusion models via hard data consistency, 2024. URL <https://arxiv.org/abs/2307.08123>.
- 829 Jiaming Song, Arash Vahdat, Morteza Mardani, and Jan Kautz. Pseudoinverse-guided diffusion
830 models for inverse problems. In *International Conference on Learning Representations*, 2023a.
831 URL https://openreview.net/forum?id=9_gsMA8MRKQ.
- 832 Jiaming Song, Qinsheng Zhang, Hongxu Yin, Morteza Mardani, Ming-Yu Liu, Jan Kautz, Yongxin
833 Chen, and Arash Vahdat. Loss-guided diffusion models for plug-and-play controllable generation.
834 In Andreas Krause, Emma Brunskill, Kyunghyun Cho, Barbara Engelhardt, Sivan Sabato, and
835 Jonathan Scarlett (eds.), *Proceedings of the 40th International Conference on Machine Learning*,
836 volume 202 of *Proceedings of Machine Learning Research*, pp. 32483–32498. PMLR, 23–29 Jul
837 2023b. URL <https://proceedings.mlr.press/v202/song23k.html>.
- 838 Yang Song, Jascha Sohl-Dickstein, Diederik P Kingma, Abhishek Kumar, Stefano Ermon, and Ben
839 Poole. Score-based generative modeling through stochastic differential equations. *arXiv preprint*
840 *arXiv:2011.13456*, 2020.
- 841 Yang Song, Liyue Shen, Lei Xing, and Stefano Ermon. Solving inverse problems in medical imaging
842 with score-based generative models. In *International Conference on Learning Representations*,
843 2022. URL <https://openreview.net/forum?id=vaRCHVj0uGI>.
- 844 Anuroop Sriram, Jure Zbontar, Tullie Murrell, Aaron Defazio, C. Zitnick, Nafissa Yakubova, Florian
845 Knoll, and Patricia Johnson. *End-to-End Variational Networks for Accelerated MRI Reconstruc-*
846 *tion*, pp. 64–73. 09 2020. ISBN 978-3-030-59712-2. doi: 10.1007/978-3-030-59713-9_7.
- 847 He Sun and Katherine L Bouman. Deep probabilistic imaging: Uncertainty quantification and multi-
848 modal solution characterization for computational imaging. In *AAAI*, pp. 2628–2637, 2021.
- 849 Yu Sun, Zhihao Xia, and Ulugbek S Kamilov. Efficient and accurate inversion of multiple scattering
850 with deep learning. *Optics express*, 26(11):14678–14688, 2018.
- 851 Yu Sun, Brendt Wohlberg, and Ulugbek S. Kamilov. An online plug-and-play algorithm for regular-
852 ized image reconstruction. *IEEE Transactions on Computational Imaging*, 5(3):395–408, 2019.
853 doi: 10.1109/TCI.2019.2893568.
- 854 Yu Sun, Zihui Wu, Yifan Chen, Berthy T. Feng, and Katherine L. Bouman. Provable probabilistic
855 imaging using score-based generative priors. *IEEE Transactions on Computational Imaging*, 10:
856 1290–1305, 2024. doi: 10.1109/TCI.2024.3449114.

- 864 Yongjin Sung, Wonshik Choi, Christopher Fang-Yen, Kamran Badizadegan, Ramachandra R Dasari,
865 and Michael S Feld. Optical diffraction tomography for high resolution live cell imaging. *Optics*
866 *express*, 17(1):266–277, 2009.
- 867 Haoyue Tang, Tian Xie, Aosong Feng, Hanyu Wang, Chenyang Zhang, and Yang Bai. Solving noisy
868 inverse problems via posterior sampling: A policy gradient view-point. In *The Symbiosis of Deep*
869 *Learning and Differential Equations III*, 2023. URL [https://openreview.net/forum?](https://openreview.net/forum?id=1phOqr675L)
870 [id=1phOqr675L](https://openreview.net/forum?id=1phOqr675L).
- 871
872 Kerem Tezcan, Christian Baumgartner, Roger Luechinger, Klaas Pruessmann, and Ender
873 Konukoglu. Mr image reconstruction using deep density priors. *IEEE Transactions on Medi-*
874 *cal Imaging*, PP:1–1, 12 2018. doi: 10.1109/TMI.2018.2887072.
- 875
876 A Richard Thompson, James M Moran, and George W Swenson. *Interferometry and synthesis in*
877 *radio astronomy*. Springer Nature, 2017.
- 878
879 L. Tian and L. Waller. 3D intensity and phase imaging from light field measurements in an LED
880 array microscope. *Optica*, 2:104–111, 2015.
- 881
882 Brian L. Trippe, Jason Yim, Doug Tischer, David Baker, Tamara Broderick, Regina Barzilay, and
883 Tommi S. Jaakkola. Diffusion probabilistic modeling of protein backbones in 3d for the motif-
884 scaffolding problem. In *The Eleventh International Conference on Learning Representations*,
885 2023. URL <https://openreview.net/forum?id=6TxBxqNME1Y>.
- 886
887 Martin Uecker, Peng Lai, M. J. Murphy, Patrick Virtue, Michael Elad, John M. Pauly, Shreyas S.
888 Vasanaawala, and Michael Lustig. Espirit—an eigenvalue approach to autocalibrating parallel
889 MRI: Where sense meets grappa. *Magnetic Resonance in Medicine*, 71, 2014.
- 890
891 Pieter Hendrik van Cittert. Die wahrscheinliche schwingungsverteilung in einer von einer lichtquelle
892 direkt oder mittels einer linse beleuchteten ebene. *Physica*, 1(1-6):201–210, 1934.
- 893
894 Singanallur V. Venkatakrishnan, Charles A. Bouman, and Brendt Wohlberg. Plug-and-play priors
895 for model based reconstruction. In *2013 IEEE Global Conference on Signal and Information*
896 *Processing*, pp. 945–948, 2013. doi: 10.1109/GlobalSIP.2013.6737048.
- 897
898 Jean Virieux and Stéphane Operto. An overview of full-waveform inversion in exploration geo-
899 physics. *Geophysics*, 74(6):WCC1–WCC26, 2009.
- 900
901 Jean Virieux, Amir Asnaashari, Romain Brossier, Ludovic Métivier, Alessandra Ribodetti, and Wei
902 Zhou. An introduction to full waveform inversion. In *Encyclopedia of exploration geophysics*,
903 pp. R1–1. Society of Exploration Geophysicists, 2017.
- 904
905 Maxime Vono, Nicolas Dobigeon, and Pierre Chainais. Split-and-augmented gibbs sam-
906 pler—application to large-scale inference problems. *IEEE Transactions on Signal Process-*
907 *ing*, 67(6):1648–1661, March 2019. ISSN 1941-0476. doi: 10.1109/tsp.2019.2894825. URL
908 <http://dx.doi.org/10.1109/TSP.2019.2894825>.
- 909
910 Shanshan Wang, Zhenghang Su, Leslie Ying, Xi Peng, Shun Zhu, Feng Liang, Dagan Feng, and
911 Dong Liang. Accelerating magnetic resonance imaging via deep learning. In *13th IEEE Inter-*
912 *national Symposium on Biomedical Imaging, ISBI 2016, Prague, Czech Republic, April 13-16,*
913 *2016*, pp. 514–517. IEEE, 2016.
- 914
915 Yinhuai Wang, Jiwen Yu, and Jian Zhang. Zero-shot image restoration using denoising diffusion
916 null-space model. In *The Eleventh International Conference on Learning Representations*, 2022.
- 917
918 David Wiesner, David Svoboda, Martin Maška, and Michal Kozubek. Cytopacq: a web-interface
919 for simulating multi-dimensional cell imaging. *Bioinformatics*, 35(21):4531–4533, 2019.
- 920
921 Emil Wolf. Three-dimensional structure determination of semi-transparent objects from holographic
922 data. *Optics communications*, 1(4):153–156, 1969.

- 918 Luhuan Wu, Brian Trippe, Christian Naesseth, David Blei, and John P Cunningham. Practi-
919 cal and asymptotically exact conditional sampling in diffusion models. In A. Oh, T. Nau-
920 mann, A. Globerson, K. Saenko, M. Hardt, and S. Levine (eds.), *Advances in Neural*
921 *Information Processing Systems*, volume 36, pp. 31372–31403. Curran Associates, Inc.,
922 2023. URL [https://proceedings.neurips.cc/paper_files/paper/2023/](https://proceedings.neurips.cc/paper_files/paper/2023/file/63e8bc7bbf1cfea36d1d1b6538aecce5-Paper-Conference.pdf)
923 [file/63e8bc7bbf1cfea36d1d1b6538aecce5-Paper-Conference.pdf](https://proceedings.neurips.cc/paper_files/paper/2023/file/63e8bc7bbf1cfea36d1d1b6538aecce5-Paper-Conference.pdf).
- 924 Zihui Wu, Yu Sun, Alex Matlock, Jiaming Liu, Lei Tian, and Ulugbek S. Kamilov. Simba: Scalable
925 inversion in optical tomography using deep denoising priors. *IEEE Journal of Selected Topics in*
926 *Signal Processing*, 14(6):1163–1175, 2020. doi: 10.1109/JSTSP.2020.2999820.
- 927 Zihui Wu, Yu Sun, Yifan Chen, Bingliang Zhang, Yisong Yue, and Katherine L Bouman. Prin-
928 cipated probabilistic imaging using diffusion models as plug-and-play priors. *arXiv preprint*
929 *arXiv:2405.18782*, 2024.
- 930 Xingyu Xu and Yuejie Chi. Provably robust score-based diffusion posterior sampling for plug-and-
931 play image reconstruction, 2024. URL <https://arxiv.org/abs/2403.17042>.
- 932 Guang Yang, Simiao Yu, Hao Dong, Gregory G. Slabaugh, Pier Luigi Dragotti, Xujiang Ye, Fangde
933 Liu, Simon R. Arridge, Jennifer Keegan, Yike Guo, and David N. Firmin. DAGAN: deep de-
934 aliasing generative adversarial networks for fast compressed sensing MRI reconstruction. *IEEE*
935 *Trans. Medical Imaging*, 37(6):1310–1321, 2018.
- 936 Yan Yang, Jian Sun, Huibin Li, and Zongben Xu. Deep admm-net for compressive sensing MRI. In
937 *Advances in Neural Information Processing Systems 29: Annual Conference on Neural Informa-*
938 *tion Processing Systems 2016, December 5-10, 2016, Barcelona, Spain*, pp. 10–18, 2016.
- 939 Jure Zbontar, Florian Knoll, Anuroop Sriram, Matthew J. Muckley, Mary Bruno, Aaron Defazio,
940 Marc Parente, Krzysztof J. Geras, Joe Katsnelson, Hersh Chandarana, Zizhao Zhang, Michal
941 Drozdal, Adriana Romero, Michael Rabbat, Pascal Vincent, James Pinkerton, Duo Wang,
942 Nafissa Yakubova, Erich Owens, C. Lawrence Zitnick, Michael P. Recht, Daniel K. Sodickson,
943 and Yvonne W. Lui. fastMRI: An open dataset and benchmarks for accelerated MRI. 2018.
- 944 Frederik Zernike. The concept of degree of coherence and its application to optical problems. *Phys-*
945 *ica*, 5(8):785–795, 1938.
- 946 Zhifang Zhan, Jian-Feng Cai, Di Guo, Yunsong Liu, Zhong Chen, and Xiaobo Qu. Fast multi-class
947 dictionaries learning with geometrical directions in MRI reconstruction. *CoRR*, abs/1503.02945,
948 2015.
- 949 Bingliang Zhang, Wenda Chu, Julius Berner, Chenlin Meng, Anima Anandkumar, and Yang Song.
950 Improving diffusion inverse problem solving with decoupled noise annealing, 2024. URL
951 <https://arxiv.org/abs/2407.01521>.
- 952 Chao Zhang, Huajian Yao, Qinya Liu, Ping Zhang, Yanhua O Yuan, Jikun Feng, and Lihua Fang.
953 Linear array ambient noise adjoint tomography reveals intense crust-mantle interactions in north
954 china craton. *Journal of Geophysical Research: Solid Earth*, 123(1):368–383, 2018a.
- 955 Cheng Zhang, Judith Bütepage, Hedvig Kjellström, and Stephan Mandt. Advances in variational
956 inference. *IEEE transactions on pattern analysis and machine intelligence*, 41(8):2008–2026,
957 2018b.
- 958 Hongkai Zheng, Wenda Chu, Austin Wang, Nikola Kovachki, Ricardo Baptista, and Yisong Yue.
959 Ensemble kalman diffusion guidance: A derivative-free method for inverse problems, 2024. URL
960 <https://arxiv.org/abs/2409.20175>.
- 961 Kevin C. Zhou and Roarke Horstmeyer. Diffraction tomography with a deep image prior. *Opt.*
962 *Express*, 28(9):12872–12896, Apr 2020. doi: 10.1364/OE.379200. URL [https://opg.](https://opg.optica.org/oe/abstract.cfm?URI=oe-28-9-12872)
963 [optica.org/oe/abstract.cfm?URI=oe-28-9-12872](https://opg.optica.org/oe/abstract.cfm?URI=oe-28-9-12872).
- 964 Bo Zhu, Jeremiah Z. Liu, Stephen F. Cauley, Bruce R. Rosen, and Matthew S. Rosen. Image
965 reconstruction by domain-transform manifold learning. *Nat.*, 555(7697):487–492, 2018.
- 966 Yuanzhi Zhu, Kai Zhang, Jingyun Liang, Jiezhong Cao, Bihan Wen, Radu Timofte, and Luc
967 Van Gool. Denoising diffusion models for plug-and-play image restoration. In *Proceedings of the*
968 *IEEE/CVF Conference on Computer Vision and Pattern Recognition*, pp. 1219–1229, 2023.

A APPENDIX

A.1 TABLES OF MAIN RESULTS

Table 3: Results on Linear inverse scattering. PSNR and SSIM of different algorithms on linear inverse scattering. Noise level $\sigma_y = 10^{-4}$.

Methods	360			180			60		
	PSNR	SSIM	Meas err (%)	PSNR	SSIM	Meas err (%)	PSNR	SSIM	Meas err (%)
Traditional									
FISTA-TV	32.126 (2.139)	0.979 (0.009)	1.23 (0.25)	26.523 (2.678)	0.914 (0.040)	2.65 (0.30)	20.938 (2.513)	0.709 (0.103)	6.05 (0.65)
PnP diffusion prior									
DDRM	32.598 (1.825)	0.929 (0.012)	1.04 (0.26)	28.080 (1.516)	0.890 (0.019)	1.57 (0.39)	20.436 (1.210)	0.545 (0.037)	3.04 (0.92)
DDNM	36.381 (1.098)	0.935 (0.017)	0.78 (0.22)	35.024 (0.993)	0.895 (0.027)	0.58 (0.16)	29.235 (3.376)	0.917 (0.022)	0.28 (0.07)
IIGDM	27.925 (3.211)	0.889 (0.072)	2.74 (1.23)	26.412 (3.430)	0.816 (0.114)	3.66 (1.79)	20.074 (2.608)	0.540 (0.198)	6.90 (3.38)
DPS	32.061 (2.163)	0.846 (0.127)	4.35 (1.19)	31.798 (2.163)	0.862 (0.123)	4.28 (1.20)	27.372 (3.415)	0.813 (0.133)	4.53 (1.31)
LGD	27.901 (2.346)	0.812 (0.037)	1.17 (0.20)	27.837 (2.337)	0.803 (0.034)	1.06 (0.16)	20.491 (3.031)	0.552 (0.077)	1.45 (0.68)
DiffPIR	34.241 (2.310)	0.988 (0.006)	1.11 (0.24)	34.010 (2.269)	0.987 (0.006)	1.04 (0.23)	26.321 (3.272)	0.918 (0.028)	1.27 (0.23)
PnP-DM	33.914 (2.054)	0.988 (0.006)	1.21 (0.25)	31.817 (2.073)	0.981 (0.008)	1.42 (0.26)	24.715 (2.874)	0.909 (0.046)	2.20 (0.34)
DAPS	34.641 (1.693)	0.957 (0.006)	1.03 (0.25)	33.160 (1.704)	0.944 (0.009)	1.11 (0.25)	25.875 (3.110)	0.885 (0.030)	1.51 (0.25)
RED-diff	36.556 (2.292)	0.981 (0.005)	0.89 (0.23)	35.411 (2.166)	0.984 (0.004)	0.87 (0.21)	27.072 (3.330)	0.935 (0.037)	1.18 (0.23)
FPS	33.242 (1.602)	0.870 (0.026)	0.70 (0.01)	29.624 (1.651)	0.710 (0.040)	0.37 (0.01)	21.323 (1.445)	0.460 (0.030)	0.15 (0.02)
MCG-diff	30.937 (1.964)	0.751 (0.029)	0.70 (0.01)	28.057 (1.672)	0.631 (0.042)	0.38 (0.01)	21.004 (1.571)	0.445 (0.028)	0.21 (0.06)

Table 4: Results on compressed sensing MRI. Mean and standard deviation are reported over 96 test cases. Underline: the best across all methods. Bold: the best across PnP DM methods.

Measurement type	$\times 4$						$\times 8$					
	Simulated (noiseless)			Raw			Simulated (noiseless)			Raw		
	PSNR \uparrow	SSIM \uparrow	Data misfit \downarrow	PSNR \uparrow	SSIM \uparrow	Data misfit \downarrow	PSNR \uparrow	SSIM \uparrow	Data-fit	PSNR \uparrow	SSIM \uparrow	Data misfit \downarrow
Traditional												
Wavelet+ ℓ_1	29.45 (1.776)	0.690 (0.121)	0.306 (0.049)	26.47 (1.508)	0.598 (0.122)	31.601 (15.286)	25.97 (1.761)	0.575 (0.105)	0.318 (0.042)	24.08 (1.602)	0.511 (0.106)	22.362 (10.733)
TV	27.03 (1.635)	0.518 (0.123)	5.748 (1.283)	26.22 (1.578)	0.509 (0.123)	32.269 (15.414)	24.12 (1.900)	0.432 (1.112)	5.087 (1.049)	23.70 (1.857)	0.427 (0.112)	23.048 (10.854)
End-to-end												
Residual UNet	32.27 (1.810)	0.808 (0.080)	-	31.70 (1.970)	0.785 (0.095)	-	29.75 (1.675)	0.750 (0.088)	-	29.36 (1.746)	0.733 (0.100)	-
E2E-VarNet	33.40 (2.097)	0.836 (0.079)	-	31.71 (2.540)	0.756 (0.102)	-	30.67 (1.761)	0.769 (0.085)	-	30.45 (1.940)	0.736 (0.103)	-
PnP diffusion prior												
CSGM	28.78 (6.173)	0.710 (0.147)	1.518 (0.433)	25.17 (6.246)	0.582 (0.167)	31.642 (15.382)	26.15 (6.383)	0.625 (0.158)	1.142 (1.078)	21.17 (8.314)	0.425 (0.192)	22.088 (10.740)
ScoreMRI	25.97 (1.681)	0.468 (0.087)	10.828 (1.731)	25.60 (1.618)	0.463 (0.086)	33.697 (15.209)	25.01 (1.526)	0.405 (0.079)	8.360 (1.381)	24.74 (1.481)	0.403 (0.080)	24.028 (10.663)
RED-diff	29.36 (7.710)	0.733 (0.131)	0.509 (0.077)	28.71 (2.755)	0.626 (0.126)	31.591 (15.368)	26.76 (6.696)	0.647 (0.124)	0.488 (0.068)	27.33 (2.441)	0.563 (0.117)	22.336 (10.838)
DiffPIR	28.31 (1.598)	0.632 (0.107)	10.545 (2.466)	27.60 (1.470)	0.624 (0.111)	34.015 (15.522)	26.78 (1.556)	0.588 (0.113)	7.787 (1.741)	26.26 (1.458)	0.590 (0.113)	24.208 (10.922)
DPS	26.13 (4.247)	0.620 (0.105)	9.900 (2.925)	25.83 (2.197)	0.548 (0.116)	35.095 (15.967)	20.82 (4.777)	0.536 (0.111)	6.737 (1.928)	23.00 (3.205)	0.507 (0.109)	24.842 (11.263)
DAPS	31.48 (1.988)	0.762 (0.089)	1.566 (0.390)	28.61 (2.197)	0.689 (0.102)	31.115 (15.497)	29.01 (1.712)	0.681 (0.098)	1.280 (0.301)	27.10 (2.034)	0.629 (0.107)	22.729 (10.926)
PnP-DM	31.80 (3.473)	0.780 (0.096)	4.701 (0.675)	27.62 (3.425)	0.679 (0.117)	32.261 (15.169)	29.33 (3.081)	0.704 (0.105)	3.421 (0.504)	25.28 (3.102)	0.607 (0.117)	22.879 (10.712)

Table 5: Generalization results on compressed sensing MRI with $\times 4$ acceleration and raw measurements. Mean and standard deviation are reported over 96 test cases.

Generalization	Vertical \rightarrow Horizontal			Knee \rightarrow Brain			$\times 4 \rightarrow \times 8$		
	PSNR \uparrow	SSIM \uparrow	Data misfit \downarrow	PSNR \uparrow	SSIM \uparrow	Data misfit \downarrow	PSNR \uparrow	SSIM \uparrow	Data misfit \downarrow
Traditional									
Wavelet+ ℓ_1	27.75 (1.683)	0.627 (0.133)	31.744 (15.362)	25.96 (1.253)	0.747 (0.026)	7.986 (0.965)	24.08 (1.602)	0.511 (0.106)	22.362 (10.733)
TV	28.18 (1.777)	0.533 (0.138)	32.311 (15.487)	25.56 (1.202)	0.686 (0.049)	8.396 (0.990)	23.70 (1.857)	0.427 (0.112)	23.048 (10.854)
End-to-end									
Residual UNet	22.06 (1.682)	0.603 (0.049)	-	30.07 (1.364)	0.881 (0.019)	-	23.93 (2.176)	0.610 (0.064)	-
E2E-VarNet	22.13 (2.925)	0.543 (0.103)	-	31.97 (1.452)	0.857 (0.038)	-	24.59 (2.012)	0.637 (0.069)	-
PnP diffusion prior									
CSGM	26.56 (3.647)	0.629 (0.129)	31.866 (15.479)	27.19 (7.521)	0.779 (0.189)	7.779 (1.043)	21.17 (8.314)	0.425 (0.192)	22.088 (10.740)
ScoreMRI	25.60 (1.647)	0.473 (0.091)	33.707 (15.274)	28.52 (0.885)	0.674 (0.045)	9.472 (0.948)	24.74 (1.481)	0.403 (0.080)	24.028 (10.663)
RED-diff	28.95 (2.480)	0.628 (0.126)	31.740 (15.421)	30.61 (0.982)	0.811 (0.048)	7.750 (0.996)	27.33 (2.441)	0.563 (0.117)	22.336 (10.838)
DiffPIR	27.93 (1.502)	0.637 (0.113)	34.188 (15.479)	27.75 (0.854)	0.823 (0.026)	10.972 (1.016)	26.26 (1.458)	0.590 (0.113)	24.208 (10.922)
DPS	26.77 (1.546)	0.571 (0.117)	35.233 (16.006)	26.77 (1.137)	0.738 (0.031)	10.806 (1.159)	23.00 (3.205)	0.507 (0.109)	24.842 (11.263)
DAPS	28.78 (2.209)	0.696 (0.105)	32.198 (15.538)	29.29 (0.911)	0.882 (0.025)	8.255 (0.986)	27.10 (2.034)	0.629 (0.107)	22.729 (10.926)
PnP-DM	27.93 (3.444)	0.689 (0.121)	32.391 (15.235)	29.96 (0.944)	0.882 (0.028)	8.789 (0.978)	25.28 (3.102)	0.607 (0.117)	22.879 (10.712)

Table 6: Results on black hole imaging. PSNR and Chi-squared of different algorithms on black hole imaging. Gain and phase noise and thermal noise are added based on EHT library.

Observation time ratio	10%				50%				100%			
	PSNR	Blur PSNR	$\bar{\chi}_{cp}^2$	$\bar{\chi}_{logos}^2$	PSNR	Blur PSNR	$\bar{\chi}_{cp}^2$	$\bar{\chi}_{logos}^2$	PSNR	Blur PSNR	$\bar{\chi}_{cp}^2$	$\bar{\chi}_{logos}^2$
Traditional												
SMILI	20.85 (2.90)	25.24 (3.86)	1.209 (0.169)	21.788 (12.491)	22.44 (3.25)	27.23 (4.35)	1.266 (0.237)	20.679 (12.612)	22.67 (3.13)	27.79 (4.02)	1.878 (0.952)	17.612 (10.299)
EHT-Imaging	22.67 (3.46)	26.66 (3.93)	1.166 (0.156)	1.240 (0.205)	23.36 (3.51)	27.22 (4.21)	1.156 (0.132)	1.154 (0.133)	24.28 (3.63)	28.57 (4.52)	1.251 (0.250)	1.259 (0.316)
PnP diffusion prior												
DPS	24.36 (3.72)	30.79 (5.75)	13.052 (43.087)	6.614 (26.789)	24.79 (3.95)	31.38 (6.37)	12.040 (45.654)	5.402 (13.036)	25.86 (3.90)	32.94 (6.19)	8.759 (37.784)	5.456 (24.185)
LGD	22.08 (3.75)	27.48 (5.09)	10.775 (21.684)	13.375 (56.397)	21.53 (3.63)	26.52 (4.84)	15.868 (38.448)	14.677 (43.822)	21.22 (3.64)	26.06 (4.98)	13.239 (17.231)	13.233 (39.107)
RED-diff	22.53 (3.02)	27.67 (4.53)	2.488 (2.925)	4.916 (13.221)	23.29 (3.64)	28.61 (5.34)	2.079 (2.254)	2.451 (4.601)	23.77 (4.13)	29.13 (6.22)	1.853 (0.938)	2.050 (2.361)
PnPDM	24.57 (3.47)	30.80 (5.22)	1.433 (0.417)	1.336 (0.478)	25.26 (3.58)	31.76 (5.50)	1.343 (0.304)	1.236 (0.332)	26.07 (3.70)	32.88 (6.02)	1.311 (0.195)	1.199 (0.221)
DAPS	23.99 (3.56)	30.10 (5.13)	1.545 (0.705)	2.253 (9.903)	24.94 (3.65)	31.57 (5.42)	1.339 (0.649)	1.737 (5.310)	25.60 (3.64)	32.78 (5.68)	1.300 (0.324)	1.229 (0.532)
DiffPIR	23.84 (3.59)	30.04 (5.03)	5.374 (3.733)	5.205 (5.536)	23.81 (4.74)	30.49 (6.53)	3.550 (1.800)	3.422 (1.880)	25.01 (4.64)	31.86 (6.56)	3.271 (1.623)	2.970 (1.202)

Table 7: Results on FWI. Mean and standard deviation are reported over 10 test cases. †: initialized from data blurred by Gaussian filters with $\sigma = 20$. *: one test case is excluded from the results due to numerical instability.

Methods	Relative L2↓	PSNR↑	SSIM↑	Data misfit↓
Traditional				
Adam	0.333 (0.086)	9.968 (2.083)	0.305 (0.120)	115.14 (52.10)
Adam†	0.089 (0.021)	21.273 (2.045)	0.679 (0.073)	15.89 (10.16)
LFBGS†	0.070 (0.023)	23.398 (2.749)	0.704 (0.077)	9.18 (6.47)
PnP diffusion prior				
DPS	0.250 (0.154)	14.111 (6.820)	0.491 (0.161)	155.08 (92.17)
LGD	0.244 (0.024)	12.288 (0.889)	0.341 (0.047)	258.47 (26.40)
DiffPIR	0.204 (0.129)	16.113 (6.962)	0.554 (0.191)	88.53 (56.91)
DAPS†	0.201 (0.103)	14.914 (4.184)	0.321 (0.067)	111.13 (71.33)
PnP-DM	0.259 (0.075)	11.983 (2.269)	0.431 (0.073)	308.84 (26.34)
REDDiff	0.319 (0.102)	10.372 (2.650)	0.280 (0.108)	94.67 (41.33)

Table 8: Results on Navier-Stokes equation. Relative ℓ_2 error of different algorithms on 2D Navier-Stokes inverse problem, reported over 10 test cases. *: one or two test cases are excluded from the results due to numerical instability.

Subsampling ratio	$\times 2$			$\times 4$			$\times 8$		
	$\sigma = 0.0$	$\sigma = 1.0$	$\sigma = 2.0$	$\sigma = 0.0$	$\sigma = 1.0$	$\sigma = 2.0$	$\sigma = 0.0$	$\sigma = 1.0$	$\sigma = 2.0$
Traditional									
EKI	0.577 (0.138)	0.609 (0.119)	0.673 (0.107)	0.579 (0.145)	0.669 (0.131)	0.805 (0.112)	0.852 (0.167)	0.940 (0.115)	1.116 (0.090)
PnP diffusion prior									
DPS-fGSG	1.687 (0.156)	1.612 (0.173)	1.454 (0.154)	1.203* (0.122)	1.209* (0.116)	1.200* (0.100)	1.246* (0.108)	1.221* (0.082)	1.260 (0.117)
DPS-cGSG	2.203* (0.314)	2.117 (0.295)	1.746 (0.191)	1.175* (0.079)	1.133* (0.095)	1.114* (0.144)	1.186* (0.117)	1.204* (0.115)	1.218 (0.113)
DPG	0.325 (0.188)	0.408* (0.173)	0.466 (0.171)	0.322 (0.200)	0.361 (0.187)	0.454 (0.207)	0.596 (0.301)	0.591 (0.262)	0.846 (0.251)
SCG	0.908 (0.600)	0.928 (0.557)	0.966 (0.546)	0.869 (0.513)	0.926 (0.546)	0.929 (0.505)	1.260 (0.135)	1.284 (0.117)	1.347 (0.141)
EnKG	0.120 (0.085)	0.191 (0.057)	0.294 (0.061)	0.115 (0.064)	0.271 (0.053)	0.522 (0.136)	0.287 (0.273)	0.546 (0.212)	0.773 (0.170)

Table 9: Table of metrics we use to capture the computation complexity of each algorithm.

Metric	Description
# Fwd _{total}	total forward model evaluations
# DM _{total}	total diffusion model evaluations
# Fwd Grad _{total}	total forward model gradient evaluations
# DM Grad _{total}	total diffusion model gradient evaluations
Cost _{total}	total runtime
# Fwd _{seq}	sequential forward model evaluations
# DM _{seq}	sequential diffusion model evaluations
# Fwd Grad _{seq}	sequential forward model gradient evaluations
# DM Grad _{seq}	sequential diffusion model gradient evaluations
Cost _{seq}	sequential runtime

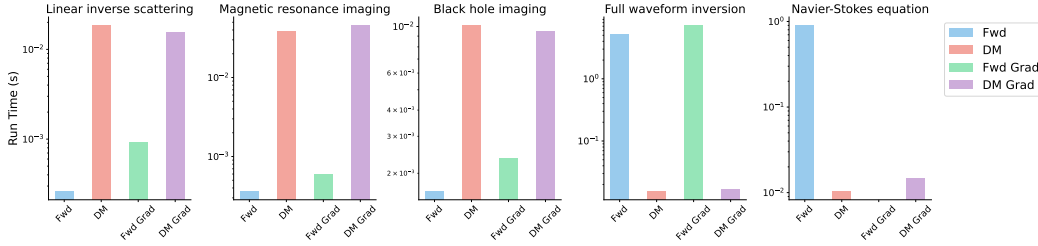


Figure 6: Computational characteristics of each forward model. Fwd: runtime of a single forward model evaluation tested on a single A100 GPU. DM: runtime of a single diffusion model evaluation. Fwd Grad: runtime of a single forward model gradient evaluation. DM Grad: runtime of a single diffusion model gradient evaluation. Note that Navier-Stokes equation only permits black-box access to the forward model so its Fwd Grad has no value.

A.2 INVERSE PROBLEM DETAILS

A.2.1 LINEAR INVERSE SCATTERING

Problem details Consider a 2D object with permittivity distribution $\epsilon(\mathbf{r})$ in a bounded sample plane $\Omega \in \mathbb{R}^2$, which is immersed in the background medium with permittivity ϵ_b . The permittivity contrast is given by $\Delta\epsilon(\mathbf{r}) = \epsilon(\mathbf{r}) - \epsilon_b$. At each time, the object is illuminated by an incident light field $\mathbf{u}_{\text{in}}(\mathbf{r})$ emitted by one of $N > 0$ transmitters, and the scattered light field $\mathbf{u}_{\text{sc}}(\mathbf{r})$ is measured by $M > 0$ receivers. We adopt the experimental setup in (Sun et al., 2018) where the transmitters and receivers are arranged along a circle $\Gamma \in \mathbb{R}^2$ that surrounds the object. Here, $\mathbf{r} := (x, y)$ denotes the spatial coordinates. Under the first Born approximation (Wolf, 1969), the interaction between the light and object is governed by the following equation

$$\mathbf{u}_{\text{tot}}(\mathbf{r}) = \mathbf{u}_{\text{in}}(\mathbf{r}) + \int_{\Omega} g(\mathbf{r} - \mathbf{r}') f(\mathbf{r}') \mathbf{u}_{\text{in}}(\mathbf{r}') d\mathbf{r}', \quad \mathbf{r} \in \Omega, \quad (13)$$

where $\mathbf{u}_{\text{tot}}(\mathbf{r})$ is the total light field, and $f(\mathbf{r}) = \frac{1}{4\pi} k^2 \Delta\epsilon(\mathbf{r})$ is the scattering potential. Here, $k = 2\pi/\lambda$ is the wavenumber in free space, and λ is the wavelength of the illumination. In the 2D space, the Green's function is given by

$$g(\mathbf{r} - \mathbf{r}') = \frac{i}{4} H_0^{(1)}(k_b \|\mathbf{r} - \mathbf{r}'\|_2) \quad (14)$$

where $k_b = \sqrt{\epsilon_b} k$ is the wavenumber of the background medium, and $H_0^{(1)}$ is the zero-order Hankel function of the first kind. Given the total field \mathbf{u}_{tot} inside the sample domain Ω , the scattered field at the sensor plane Γ is given by

$$\mathbf{u}_{\text{sc}}(\mathbf{r}) = \int_{\Omega} g(\mathbf{r} - \mathbf{r}') f(\mathbf{r}') \mathbf{u}_{\text{tot}}(\mathbf{r}') d\mathbf{r}', \quad \mathbf{r} \in \Gamma. \quad (15)$$

Note that \mathbf{r} denotes the sensor location in Γ , and the integral is computed over Ω .

By discretizing equations (13) and (15), we obtain a vectorized system that describes the linear inverse scattering problem. We denote the 2D vectorized permittivity distribution of the object by $\mathbf{z} := f(\mathbf{r})$, and the corresponding measurement by $\mathbf{y}_{\text{sc}} = \mathbf{u}_{\text{sc}}(\mathbf{r})$ for notation consistency.

The forward model can thus be written as

$$\mathbf{y}_{\text{sc}} = \mathbf{H}(\mathbf{u}_{\text{tot}} \odot \mathbf{z}) + \mathbf{e} = \mathbf{A}\mathbf{z} + \mathbf{e}, \quad (16)$$

where $\mathbf{u}_{\text{tot}} = \mathbf{G}(\mathbf{u}_{\text{in}} \odot \mathbf{z})$, matrices \mathbf{G} and \mathbf{H} are discretizations of the Green's function at Γ and Ω , respectively, and $\mathbf{A} := \mathbf{H}\text{diag}(\mathbf{u}_{\text{tot}})$. We split and concatenate the real and imaginary part of \mathbf{A} , and pre-compute the singular value decomposition of \mathbf{A} to facilitate the plug-and-play diffusion methods that exploit SVD of linear inverse problems.

We set the physical size of test images to $18\text{cm} \times 18\text{cm}$, and the wavelength of the illumination to $\lambda = 0.84\text{cm}$ as specified in (Sun et al., 2019). The forward model consists of $N = 20$ transmitters, placed uniformly on a circle of radius $R = 1.6\text{m}$. We further assume the permittivity of the background medium as $\epsilon_b = 1$. We specify the number of receivers to be $M = 360, 180, 60$ in our experiments.

Related work Linear inverse scattering aims to reconstruct the spatial distribution of an object’s dielectric permittivity from the measurements of the light it scatters (Wolf, 1969; Kak & Slaney, 2001). This problem arises in various applications, such as ultrasound imaging (Bronstein et al., 2002), optical microscopy (Choi et al., 2007; Sung et al., 2009), and digital holography (Brady et al., 2009). Due to the physical constraints on the number and placement of sensors, the problem is often ill-posed, as the scattered light field is undersampled. Linear inverse scattering is commonly formulated as a linear inverse problem using scattering models based on the first Born (Wolf, 1969) or Rytov (Devaney, 1981) approximations. These models enable efficient computation and facilitate the use of convex optimization algorithms. On the other hand, nonlinear approaches have been developed to image strongly scattering objects (Kamilov et al., 2015; Tian & Waller, 2015; Ma et al., 2018; Liu et al., 2018; Chen et al., 2020), although these methods generally have a higher computational complexity. Deep learning-based methods have also been explored for linear inverse scattering. A common approach is to train convolutional neural networks (CNNs) to directly invert the scattering process by learning an inverse mapping from the measurements to permittivity distribution (Sun et al., 2018; Li et al., 2018a;c; Wu et al., 2020). Recent research has extended these efforts to more advanced deep learning techniques, such as neural fields (Liu et al., 2022; Cao et al., 2024) and deep image priors (Zhou & Horstmeyer, 2020).

A.2.2 COMPRESSED SENSING MULTI-COIL MRI

Problem details We use the raw multi-coil k -space data from the fastMRI knee dataset (Zbontar et al., 2018). We then estimate the coil sensitivity maps of each slice using the `ESPIRiT` (Uecker et al., 2014) method implemented in `sigPy`³. Since different volumes in the dataset have different shapes, we adopt the preprocessing procedure in (Jalal et al., 2021), leading to images with 320×320 shape. The ground truth image is given by calculating the magnitude image of the Minimum Variance Unbiased Estimator (MVUE), which is used for all numbers reported in Table 4 and Table 5. The MVUE images are also used as ground truths for training the end-to-end deep learning methods Residual UNet and E2E-VarNet (Sriram et al., 2020).

Related work Compressed sensing magnetic resonance imaging (CS-MRI) is a medical imaging technology that enables high-resolution visualization of human tissues with faster acquisition time than traditional MRI (Lustig et al., 2007). Instead of fully sampling the measurement space (a.k.a. k -space), CS-MRI only takes sparse measurements and then solves an inverse problem that recovers the underlying image (Lustig et al., 2008). The traditional approach is to solve a regularized optimization problem that involves a data-fit term and a regularization term, such as the total variation (TV) (Bouman & Sauer, 1993), and the ℓ_1 -norm after a sparsifying transformation, such as Wavelet transform (Ma et al., 2008) and dictionary decomposition (Ravishankar & Bresler, 2011; Huang et al., 2014; Zhan et al., 2015)). End-to-end deep learning methods have also demonstrated strong performance in MRI reconstruction. Prior works have proposed unrolled networks (Yang et al., 2016; Hammernik et al., 2017; Aggarwal et al., 2017; Schlemper et al., 2018; Liu et al., 2021), UNet-based networks (Lee et al., 2017; Hyun et al., 2017), GAN-based networks (Yang et al., 2018; Quan et al., 2018), among others (Wang et al., 2016; Zhu et al., 2018; Tezcan et al., 2018; Luo et al., 2019; Liu et al., 2020). These learning methods have achieved state-of-the-art performance on the fastMRI dataset (Zbontar et al., 2018). Another line of work is to employ image denoisers as plug-and-play prior (Liu et al., 2020; Jalal et al., 2021; Sun et al., 2024). Recently, diffusion model-based methods have been designed for CS-MRI reconstruction (Chung & Ye, 2022; Luo et al., 2022; Chung et al., 2023).

A.2.3 BLACK HOLE IMAGING

Problem details Measurements for black hole imaging are obtained using Very Long Baseline Interferometry (VLBI). The cross-correlation of the recorded scalar electric fields at two telescopes, referred to as the (ideal) *visibility*, is related to the ideal source image \mathbf{z} through a Fourier transform, as given by the van Cittert-Zernike theorem:

$$\mathbf{I}_{(a,b)}^t(\mathbf{z}) = \int_{\rho} \int_{\delta} e^{-i2\pi(u_{(a,b)}^t \rho + v_{(a,b)}^t \delta)} \mathbf{z}(\rho, \delta) d\rho d\delta. \quad (17)$$

³<https://github.com/mikgroup/sigpy>

Here, (ρ, δ) denotes the angular coordinates of the source image, and $(u_{(a,b)}^t, v_{(a,b)}^t)$ is the dimensionless baseline vector between two telescopes (a, b) , orthogonal to the source direction. In practice, these measurements can be time-averaged over short intervals.

Due to atmospheric turbulence and instrumental calibration errors, the observed visibilities are corrupted by amplitude and phase errors, along with additive Gaussian thermal noise (EHTC, 2019a; Sun et al., 2024):

$$V_{(a,b)}^t = g_a^t g_b^t e^{-i(\phi_a^t - \phi_b^t)} \mathbf{I}_{(a,b)}^t(\mathbf{z}) + \boldsymbol{\eta}_{(a,b)}^t. \quad (18)$$

Note that there are three main sources of noise at time t : gain errors g_a^t, g_b^t , phase errors ϕ_a^t, ϕ_b^t , and baseline-based additive white Gaussian noise $\boldsymbol{\eta}_{(a,b)}^t$. While the phase of the visibility cannot be directly used due to phase errors, the product of three visibilities among any set of three telescopes, known as the *bispectrum*, can be computed to retain useful information. Specifically, the phase of the bispectrum, termed the *closure phase*, effectively cancels out phase errors in the observed visibilities. Similarly, a strategy can be employed to cancel out amplitude gain errors and extract information from the visibility amplitude (Blackburn et al., 2020). Formally, these quantities are defined as:

$$\begin{aligned} \mathbf{y}_{t,(a,b,c)}^{\text{cp}} &= \angle(V_{(a,b)}^t V_{(b,c)}^t V_{(a,c)}^t), \\ \mathbf{y}_{t,(a,b,c)}^{\text{logca}} &= \log \left(\frac{|V_{(a,b)}^t| |V_{(c,d)}^t|}{|V_{(a,c)}^t| |V_{(b,d)}^t|} \right). \end{aligned} \quad (19)$$

Here, \angle denotes the complex angle, and $|\cdot|$ computes the complex amplitude. For a total of M telescopes, the number of closure phase measurements $\mathbf{y}_{t,(a,b,c)}^{\text{cp}}$ at time t is $\frac{(M-1)(M-2)}{2}$, and the number of log closure amplitude measurements $\mathbf{y}_{t,(a,b,c)}^{\text{logca}}$ is $\frac{M(M-3)}{2}$, after accounting for redundancy. To avoid having to solve for the calibration terms, black hole imaging methods can constrain closure quantities during inference. Since closure quantities are nonlinear transformations of the visibilities, the forward model in black hole imaging then becomes non-convex.

The total flux of the image source, representing the DC component of the Fourier transform, is given by:

$$\mathbf{y}^{\text{flux}} = G^{\text{flux}}(\mathbf{z}) = \int_{\rho} \int_{\delta} \mathbf{z}(\rho, \delta) d\rho d\delta. \quad (20)$$

To aggregate data over time intervals and telescope combinations, the forward model of black hole imaging can be expressed as:

$$\mathbf{y} = G(\mathbf{z}, \xi) = (G^{\text{cp}}(\mathbf{z}), G^{\text{logca}}(\mathbf{z}), G^{\text{flux}}(\mathbf{z})) = (\mathbf{y}^{\text{cp}}, \mathbf{y}^{\text{logca}}, \mathbf{y}^{\text{flux}}), \quad (21)$$

The data consistency is typically assessed using the χ^2 statistic:

$$\begin{aligned} \mathcal{L}(\mathbf{y} | \mathbf{z}) &= \chi_{\text{cp}}^2 + \chi_{\text{logca}}^2 + \chi_{\text{flux}}^2 \\ &= \frac{1}{N_{\text{cp}}} \left\| \frac{G^{\text{cp}}(\mathbf{z}) - \mathbf{y}^{\text{cp}}}{\sigma_{\text{cp}}} \right\|^2 + \frac{1}{N_{\text{logca}}} \left\| \frac{G^{\text{logca}}(\mathbf{z}) - \mathbf{y}^{\text{logca}}}{\sigma_{\text{logca}}} \right\|^2 + \left\| \frac{G^{\text{flux}}(\mathbf{z}) - \mathbf{y}^{\text{flux}}}{\sigma_{\text{flux}}} \right\|^2. \end{aligned} \quad (22)$$

Here, σ_{cp} , σ_{logca} , and σ_{flux} are the estimated standard deviations of the measured closure phase, log closure amplitude, and flux, respectively. Additionally, N_{cp} and N_{logca} represent the total number of time intervals and telescope combinations for the closure phase and log closure amplitude measurements.

Related work The Event Horizon Telescope (EHT) Collaboration aims to image black holes using a global network of radio telescopes operating at around a 1 mm wavelength. Through very-long-baseline interferometry (VLBI) (Thompson et al., 2017), data from these telescopes are synchronized to obtain measurements in 2D Fourier space of the sky’s image, known as *visibilities* (van Cittert, 1934; Zernike, 1938). These measurements only sparsely cover the low-spatial-frequency space and are corrupted by instrument noise and atmospheric turbulence, making the inverse problem of image recovery ill-posed. Using traditional imaging techniques, the EHT Collaboration has successfully imaged the supermassive black holes M87* (EHTC, 2019b; 2024) and SgrA* (EHTC, 2022). The classical imaging algorithm is CLEAN (Högbom, 1974; Clark, 1980), as implemented in the DIFMAP (Shepherd, 1997; 2011) software. DIFMAP is an inverse modeling approach that starts

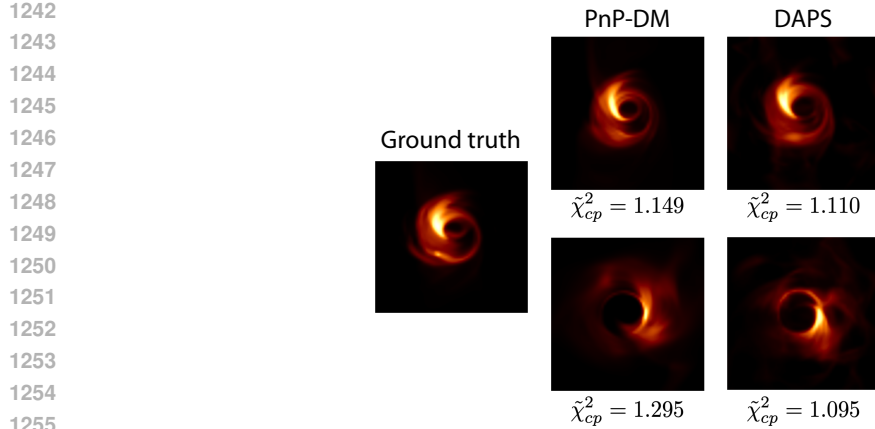


Figure 7: Multi-modal example on black hole imaging. The image shows two systematic modes discovered by DAPS and PnP-DM

with the “dirty” image (given by the inverse Fourier transform of the visibilities) and iteratively deconvolves the image with an estimate point-spread function to “clean” the image. Since DIFMAP often requires a human-in-the-loop, we chose not to present results from DIFMAP. The EHT has also developed and used regularized maximum-likelihood approaches, namely `eht-imaging` (Chael et al., 2016; 2018; 2019) and `SMILI` (Akiyama et al., 2017b;a; 2019). Although they regularize and optimize the image differently (EHTC, 2019b), `eht-imaging` and `SMILI` both iteratively update an estimated image to agree with the measured data and regularization assumptions. Because of the simple regularization they choose to use, these baseline methods are limited in the amount of visual detail they can recover and do not recover detail far beyond the intrinsic resolution of the measurements. Some deep-learning-based regularization approaches have been proposed for VLBI (Feng et al., 2024; Feng & Bouman, 2024; Dia et al., 2023), but most plug-and-play inverse diffusion solvers have not been validated on black hole imaging.

Multi-modal observation As previously discussed, the non-convex and sparse measurement characteristics of black hole imaging cause the inverse problem to exhibit multi-modal behavior. Consequently, the resulting samples may follow systematic modes that, while potentially quite different from the true source images, fit the observational data well and exhibit high prior likelihood. Figure 7 illustrates two such modes discovered by DAPS and PnP-DM. This multi-modal behavior has not been extensively formulated or discussed in previous literature, and we believe it represents a phenomenon worthy of further investigation.

A.2.4 FULL WAVEFORM INVERSION

Problem details In Equation (8), solving for the pressure wavefield \mathbf{u} given the slowness \mathbf{z} and source term \mathbf{q}_s defines the forward modeling process. We use an open-source software, `Devito` (Louboutin et al., 2019), for both forward modeling and adjoint FWI. We use a 128×128 mesh to discretize a physical domain of $2.54 \text{ km} \times 1.27 \text{ km}$, with a horizontal spacing of 20 m and a vertical spacing of 10 m. The time step is set to 0.001 s which satisfies the Courant–Friedrichs–Lewy (CFL) condition (Courant et al., 1967). We use a Ricker wavelet with a central frequency of 5 Hz to excite the wavefield and model it for 1 s. The natural boundary condition is set for the top boundary (free surface) which will generate reflected waves, while the absorbing boundary condition (Clayton & Engquist, 1977) is set for the rest boundaries to avoid artificial reflections. The absorbing boundary width is set to 80 grid points.

Inferring \mathbf{z} from observed data at receivers defines the inverse problem. We put 129 receivers evenly near the free surface (at a depth of 10 m) to model a realistic scenario. We excite 16 sources evenly at a depth of 1270 m. This source-receiver geometry is designed for the entire physical medium to be sampled by seismic waves, making it theoretically feasible to invert for \mathbf{m} . `Devito` uses the adjoint-state method to estimate the gradient $\nabla \Phi_s(\mathbf{m})$ by cross-correlating the forward and adjoint

wavefields at zero time lag (Plessix, 2006):

$$\nabla\Phi_s(\mathbf{m}) = \sum_{t=1}^{N_t} \mathbf{u}[t]\mathbf{v}_{tt}[t], \quad (23)$$

where N_t is the number of time steps. The adjoint wavefield \mathbf{v} is generated by treating the receivers as sources and back-propagating the residual $\delta\mathbf{d}$ between the modeled and observed data into the model:

$$\begin{aligned} \mathbf{A}^T(\mathbf{m})\mathbf{v} &= \delta\mathbf{d}, \\ \delta\mathbf{d} &= \mathbf{P}_r\mathbf{u} - \mathbf{d}. \end{aligned} \quad (24)$$

This process is repeated for each source location, and the gradients are summed to update the parameter of interest.

Traditional baselines One baseline is the Adam optimization algorithm (Kingma, 2014). We implement the Adam optimizer with a learning rate of 0.02 with the learning rate decay to minimize the data misfit term. For the traditional method, the initial model is a smoothed version of the true model, using a Gaussian filter with $\sigma = 20$. We perform the inversion for 300 iterations.

A.2.5 NAVIER-STOKES

Forward modeling The following 2D Navier-Stokes equation for a viscous, incompressible fluid in vorticity form on a torus defines the forward model.

$$\begin{aligned} \partial_t \mathbf{w}(\mathbf{x}, t) + \mathbf{u}(\mathbf{x}, t) \cdot \nabla \mathbf{w}(\mathbf{x}, t) &= \nu \Delta \mathbf{w}(\mathbf{x}, t) + f(\mathbf{x}), & \mathbf{x} \in (0, 2\pi)^2, t \in (0, T] \\ \nabla \cdot \mathbf{u}(\mathbf{x}, t) &= 0, & \mathbf{x} \in (0, 2\pi)^2, t \in [0, T] \\ \mathbf{w}(\mathbf{x}, 0) &= \mathbf{w}_0(\mathbf{x}), & \mathbf{x} \in (0, 2\pi)^2 \end{aligned} \quad (25)$$

where $\mathbf{u} \in C([0, T]; H_{\text{per}}^r((0, 2\pi)^2; \mathbb{R}^2))$ for any $r > 0$ is the velocity field, $\mathbf{w} = \nabla \times \mathbf{u}$ is the vorticity, $\mathbf{w}_0 \in L_{\text{per}}^2((0, 2\pi)^2; \mathbb{R})$ is the initial vorticity, $\nu \in \mathbb{R}_+$ is the viscosity coefficient, and $f \in L_{\text{per}}^2((0, 2\pi)^2; \mathbb{R})$ is the forcing function. The solution operator $\mathcal{G} : \mathbf{w}_0 \rightarrow \mathbf{w}_T$ is defined as the operator mapping the vorticity from the initial vorticity to the vorticity at time T . We implement the forward model using a pseudo-spectral solver with adaptive time stepping (He & Sun, 2007).

Dataset To generate the training and test samples, we first draw independent identically distributed samples from the Gaussian random field $\mathcal{N}(0, (-\Delta + 9\mathbf{I})^{-4})$, where Δ denotes the negative Laplacian. Then, we evolve them according to Equation 9 for 5 time units to get the final vorticity field, which generates an empirical distribution of the vorticity field with rich flow features. We set the forcing function $f(\mathbf{x}) = -4 \cos(4\mathbf{x}_2)$.

A.3 PRETRAINED DIFFUSION MODEL DETAILS

We train diffusion models following the pipeline from (Karras et al., 2022), using UNet architectures from (Dhariwal & Nichol, 2021) and (Song et al., 2020). Detailed network configurations can be found in Table 10.

Table 10: Model Card for pre-trained diffusion models.

	Inverse scattering	Black hole	MRI	FWI	2D Navier-Stokes
Input resolution	128×128	64×64	$2 \times 320 \times 320$	128×128	128×128
# Attention blocks in encoder/decoder	5	3	5	5	5
# Residual blocks per resolution	1	1	1	1	1
Attention resolutions	{16}	{16}	{16}	{16}	{16}
# Parameters	26.8M	20.0M	26.0M	26.8M	26.8M
# Training steps	50,000	50,000	100,000	50,000	50,000

A.4 ALGORITHMS AND PARAMETER CHOICES

A.4.1 PROBLEM-SPECIFIC BASELINES

Black hole imaging We use `SMILI` (Akiyama et al., 2017b;a; 2019) and `eht-imaging` (Chael et al., 2016; 2018; 2019) as our baseline methods. To ensure compatibility with the default hyperparameters of these methods, we preprocess the test dataset accordingly.

Full waveform inversion A classic baseline for full waveform inversion is the `Adam` optimization algorithm (Kingma, 2014). We implement the `Adam` optimizer with a learning rate of 0.02 with the learning rate decay to minimize the data misfit term. For the traditional method, the initialization is a smoothed version of the ground truth, which is blurred using a Gaussian filter with $\sigma = 20$. We perform the inversion for 300 iterations. The second baseline we consider is `LBFGS`. We set the maximum iteration to 5 and perform 100 global update steps with a Wolfe line search.

Linear inverse scattering We include `FISTA-TV` (Sun et al., 2019) as a traditional optimization-based method. We set batch size $B = 20$ and $\tau = 5 \times 10^{-7}$ for all experiments.

Compressed sensing multi-coil MRI We utilize both traditional methods, such as `Wavelet+ ℓ_1` (Lustig et al., 2007; Lustig et al., 2008) and `TV`, as well as end-to-end models like `Residual UNet` and `E2E-VarNet` (Sriram et al., 2020). For the traditional methods, we apply the same hyperparameter search strategy for fine-tuning, while the end-to-end models are trained using the `Adam` optimizer with a learning rate of $1e - 4$ until convergence.

Navier-Stokes equation We implement the traditional Ensemble Kalman inversion with 2048 particles, 500 update steps, and adaptive step size used in (Kovachki & Stuart, 2019; Garbuno-Inigo et al., 2020). `DPS-fGSG` and `DPS-cGSG` are natural `DPS` extensions that replace gradient by zeroth-order gradient estimation. More specifically, we use forward and central Gaussian Smoothed Gradient estimation technique (Berahas et al., 2022).

A.4.2 HYPERPARAMETER SELECTION

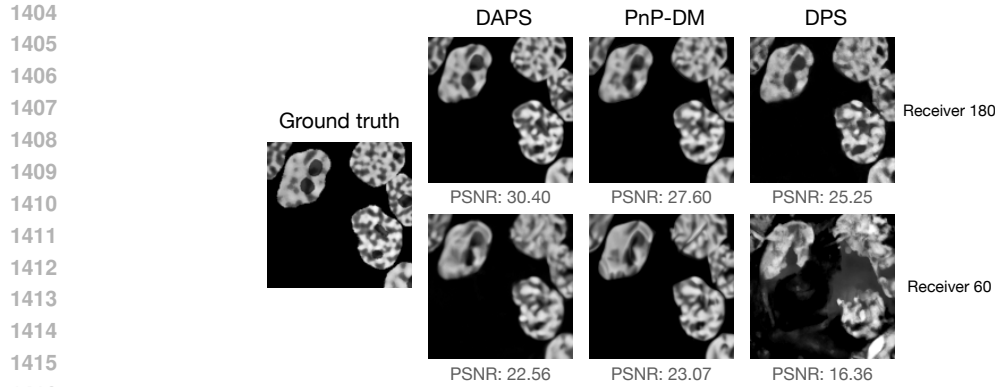
To ensure sufficient tuning of the hyperparameters for each algorithm, we employ a hybrid strategy combining grid search with Bayesian optimization and early termination technique, using a small validation dataset. Specifically, we first perform a coarse grid search to narrow down the search space and then apply Bayesian optimization. For problems where the forward model is fast such as linear inverse scattering, MRI, and black hole imaging, we conduct 50-100 iterations of Bayesian optimization to select the best hyperparameters. For computationally intensive problems such as full waveform inversion and Navier-Stokes equation, we use 10-30 iterations of Bayesian optimization combined with an early termination technique (Li et al., 2018b), based on data misfit. The details of the search spaces for Bayesian optimization and the optimized hyperparameter choices are listed in Table 11.

B FUTURE DIRECTION

In this section, we outline a few future directions for benchmarking PnPDP methods for solving inverse problems.

Robustness to forward model mismatch In our paper, we only consider the setting where the forward model is exact and explicit. However, in real-world scenarios, the forward model is often an approximation. Studying the robustness of algorithms when there is a mismatch between the assumed and actual forward model would be an essential step toward their practical deployment. This includes exploring how algorithms handle noisy or imperfect forward model representations.

Robustness to prior mismatch The robustness of a diffusion prior often depends on two key factors: the degree of ill-posedness and the balance between the prior and the observation in the sampling algorithm. Highly ill-posed tasks, such as black hole imaging, require a more in-distribution prior to achieve reasonable results, whereas less ill-posed tasks, such as linear inverse scattering, are



1417 Figure 8: Robustness to a human face prior in linear inverse scattering shows that methods requiring
 1418 more data gradient steps tend to generalize better than those that prioritize the prior more.

1419

1420

1421 less sensitive to this requirement. Regarding the balance between prior and observation, methods
 1422 like DAPS and PnP-DM, which incorporate more data gradient steps, tend to be more robust to out-
 1423 of-distribution prior than methods like DPS. We include a preliminary discussion on this in Figure 8
 1424 presents a comparison of the robustness of different algorithms in the linear inverse scattering using
 1425 a prior trained on FFHQ 256×256 human face images. We will pursue further exploration in this
 1426 direction in the future.

1426

1427

1428 **Multi-modal posterior** In this work, we focus exclusively on scenarios where the ground truth is
 1429 unimodal. However, some real-world inverse problems might exhibit posteriors that are inherently
 1430 multimodal, reflecting multiple plausible solutions given the observations. Developing systematic
 1431 benchmarks to evaluate how accurately different PnPDP methods can capture such multimodal pos-
 1432 teriors is an interesting and challenging research question.

1432

1433

1434

1435

1436

1437

1438

1439

1440

1441

1442

1443

1444

1445

1446

1447

1448

1449

1450

1451

1452

1453

1454

1455

1456

1457

Table 11: Hyperparameter search space and final choices of the diffusion-model-based algorithms on all five inverse problems. Columns marked with task names present the chosen values for the reported main results in Appendix A.1. These values are selected by a hybrid hyperparameter search strategy described in Appendix A.4.2.

Methods/Parameters	Search space	Linear inverse scattering (360 / 180 / 60)	Black hole	MRI (Sim. / Raw)	FWI	2D Navier-Stokes
DPS						
Guidance scale	$[10^{-3}, 10^3]$	280/380/625	0.003	0.589/0.428	10^{-2}	-
LGD						
Guidance scale	$[10^{-3}, 10^4]$	3200/6400/13000	0.0082	-	11.73	-
# MC samples	[1, 20]	20	8	-	5	-
REDDiff						
Learning rate	$[10^{-4}, 1.0]$	0.04	0.05	$4 \times 10^{-2} / 2.96 \times 10^{-2}$	0.01	-
Regularization λ_{base}	$[10^{-3}, 1.0]$	0.0005	0.25	$2.33 \times 10^{-1} / 2.72 \times 10^{-3}$	0.1	-
Regularization schedule	constant, linear, sqrt	constant	constant	sqrt	linear	-
Gradient weight	$[10^{-2}, 10^2]$	1500	0.0004	$6.68 \times 10^1 / 1.7 \times 10^{-2}$	1	-
DiffPIR						
# sampling steps	{200, 400, ..., 1000}	200	1000	1000	1000	-
Regularization λ	$[1, 10^5]$	$4 \times 10^{-4} / 2 \times 10^{-4} / 10^{-4}$	113.6	163 / 1.31	80.6	-
Stochasticity ζ	$[10^{-5}, 1]$	1	0.34	0.114 / 0.478	0.11	-
Noise level σ_y	$[10^{-2}, 10^1]$	0.01	1.4	$1.05 \times 10^{-2} / 1.36 \times 10^{-1}$	0.28	-
PnPDM						
Annealing step	[50, 200]	100	100	100	150	-
Annealing sigma max	[10, 50]	10	10	10	25	-
Annealing decay rate	[0.60, 0.99]	0.9	0.93	0.93	0.99	-
Langevin step size	$[10^{-6}, 10^{-3}]$	$2 \times 10^{-5} / 4 \times 10^{-5} / 10^{-4}$	10^{-5}	10^{-6}	3×10^{-4}	-
Langevin step number	[10, 500]	200	200	200	10	-
Noise level	$[10^{-4}, 10^1]$	10^{-4}	1	$1.02 \times 10^{-3} / 1.15 \times 10^{-2}$	1	-
DAPS						
Annealing step	[50, 200]	200	100	200	150	-
Diffusion step	[1, 10]	10	5	5	5	-
Langevin step size	$[10^{-6}, 10^{-3}]$	$4 \times 10^{-5} / 8 \times 10^{-5} / 2 \times 10^{-4}$	10^{-4}	$1.03 \times 10^{-5} / 1.52 \times 10^{-5}$	3×10^{-4}	-
Langevin step number	[10, 500]	50	20	100	50	-
Noise level	$[10^{-4}, 10^1]$	10^{-4}	1	$1.63 \times 10^{-3} / 4.77 \times 10^{-3}$	1	-
Step size decay	[0.1, 1]	1/1/0.5	1	1	1	-
DDRM						
Stochasticity η	[0, 1]	0.85	-	-	-	-
DDNM						
Stochasticity η	[0, 1]	0.95	-	-	-	-
# time-travel steps L	[0, 5]	1	-	-	-	-
IGDM						
Stochasticity η	[0, 1]	0.2	-	-	-	-
FPS						
Stochasticity η	[0, 1]	0.9	-	-	-	-
# particles	[1, 20]	20	-	-	-	-
MCG-diff						
# particles	[1, 64]	16	-	-	-	-
DPS-fGSG						
Guidance scale	$[10^{-2}, 10^2]$	-	-	-	-	0.1
DPS-cGSG						
Guidance scale	$[10^{-2}, 10^2]$	-	-	-	-	0.1
DPG						
# MC samples	{1000, 2000, ..., 6000}	-	-	-	-	4000
Guidance scale	$[10^{-1}, 10^3]$	-	-	-	-	64
SCG						
# MC samples	{128, 256, 512}	-	-	-	-	512
EnKG						
Guidance scale	{1.0, 2.0, 4.0}	-	-	-	-	2.0
# particles	{512, 1024, 2048}	-	-	-	-	2048